ADVANCED MATERIALS
www.advmat.de

Check for updates

Harnessing the Metal–Insulator Transition of VO_2 in Neuromorphic Computing

Parker Schofield, Adelaide Bradicich, Rebeca M. Gurrola, Yuwei Zhang, Timothy D. Brown, Matt Pharr, Patrick J. Shamberger, and Sarbajit Banerjee**

Future-generation neuromorphic computing seeks to overcome the limitations of von Neumann architectures by colocating logic and memory functions, thereby emulating the function of neurons and synapses in the human brain. Despite remarkable demonstrations of high-fidelity neuronal emulation, the predictive design of neuromorphic circuits starting from knowledge of material transformations remains challenging. VO_2 is an attractive candidate since it manifests a near-room-temperature, discontinuous, and hysteretic metal–insulator transition. The transition provides a nonlinear dynamical response to input signals, as needed to construct neuronal circuit elements. Strategies for tuning the transformation characteristics of VO_2 based on modification of material properties, interfacial structure, and field couplings, are discussed. Dynamical modulation of transformation characteristics through in situ processing is discussed as a means of imbuing synaptic function. Mechanistic understanding of site-selective modification; external, epitaxial, and chemical strain; defect dynamics; and interfacial field coupling in modifying local atomistic structure, the implications therein for electronic structure, and ultimately, the tuning of transformation characteristics, is emphasized. Opportunities are highlighted for inverse design and for using design principles related to thermodynamics and kinetics of electronic transitions learned from VO_2 to inform the design of new Mott materials, as well as to go beyond energy-efficient computation to manifest intelligence.

1. Introduction

The rise of Artificial Intelligence (AI) is fundamentally transforming the engines of scientific discovery, technological innovation, and precision manufacturing that are at the heart of modern economies.[1] While AI affords opportunities for accelerating technological advancements and hope for new insights into intractable scientific problems, major speedbumps ahead include exorbitant computational costs, especially in the training of high-performing models, as well as the lack of physical interpretability.[2,3] Exponential increases in computing are required to handle the impending deluge of data—projected to increase from 50 to 10^6 zettabytes in the next two decades—and to embed physical intelligence from the edge-of-the-internet to the heart of the cloud.[4,5] Conventional computing is approaching fundamental limits imposed by the thermodynamics of charge-transfer mechanisms in electrostatically modulated semiconductors and by the von Neumann architectural bottleneck of shuttling data between separate memory and processing units.[6–9] For many decades, semiconductor manufacturers kept pace with computing demands by downsizing transistors (Moore's scaling);[10,11] however, the performance of complementary metal-oxide semiconductor (CMOS) components is fundamentally limited by the room-temperature Fermi–Dirac distribution of electron energies, which, for instance, limits the steepness of the subthreshold voltage swing to 60 mV per decade increase in current across a transistor channel.[7–9] Additional limitations arise from the breakdown of Dennard scaling of power density, which has the consequence of sharply reducing the proportion of a silicon chip that is switched at full frequency with each process generation.[12] As a result, increasingly larger areas of a chip are left idle or underutilized, the so-called "dark silicon" problem.[13] Indeed, with the data deluge having only just begun, Moore's law scaling nearing saturation, and traditional von Neumann architectures facing major roadblocks, computing stands at a watershed.

It is thus necessary to consider computing from wider material and architectural perspectives. In traditional von Neumann

P. Schofield, S. Banerjee
Department of Chemistry
Texas A&M University
College Station, TX 77843, USA
E-mail: banerjee@chem.tamu.edu

P. Schofield, A. Bradicich, R. M. Gurrola, P. J. Shamberger, S. Banerjee
Department of Materials Science and Engineering
Texas A&M University
College Station, TX 77843, USA
E-mail: patrick.shamberger@tamu.edu

Y. Zhang, M. Pharr
Department of Mechanical Engineering
Texas A&M University
College Station, TX 77843, USA

T. D. Brown
Sandia National Laboratories
Livermore, CA 94551, USA

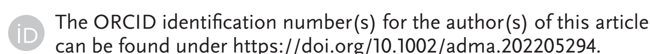
The ORCID identification number(s) for the author(s) of this article can be found under https://doi.org/10.1002/adma.202205294.

DOI: 10.1002/adma.202205294

 © 2022 Wiley-VCH GmbH

ADVANCED MATERIALS
www.advmat.de

architectures, hardware supports a computing core consisting of a random access memory (RAM) unit, which holds data for active, ongoing processes, and a central processing unit, which performs the arithmetic of calculations in a logic subunit in addition to managing calculation instructions and data retrieval and recording to RAM. Much of the time and energy spent in computing pertains to hardware communication relays between the central processing unit and RAM.[14] This so-called "von Neumann bottleneck" has been discussed for decades with the most straightforward solutions being: 1) improving the efficiency of circuitry and circuitry components (which worked well until the end of Moore's and Dennard scaling) and 2) adopting altogether new computing architectures.

Nature presents a notable exemplar for a low-voltage, "dark," highly energy economical architecture that avoids the separation of working memory and processing components. Although the human brain itself comprises a multitude of subunits, it is uniquely capable of storing, processing, and transmitting information within a singular fabric.[6,15–17] Neurons require much less energy to process and transmit data as compared to Si architectures as a result of their high synaptic interconnection and precisely correlated electrical spikes.[15,18] By altering the potency of interaction between pre- and postsynaptic neurons (synaptic weight), the brain essentially holds multiple states in memory, which can be conveyed across synapses by neurotransmitters.[19] As a computing design principle, this is referred to as a neuromorphic computing architecture, which the European Human Brain Project defines as "implementation of aspects of biological neural networks as analogue or digital copies on electronic circuits."[20]

The emerging discipline of neuromorphic computing seeks to draw inspiration from processes observed in the brain, functionally reimagining neurons as materials colocating memory and processing capabilities without breaking communication, ideally with synaptic-neuronal-interconnect functional reconfigurability.[21,22] Although neuromorphic computation can be implemented in conventional Si circuitry using neural network algorithms featuring variable potency of interlayer weighting coefficients, this approach is prohibitively expensive with regards to transistor count, time, and energy usage[7,17,23–28] Many hundreds to thousands of transistors are required to simulate the analog integration, thresholding, and firing processes of neurons that could instead be emulated by one or two nonlinear dynamical circuit elements.[29–33] Thus, intense interest has focused on the design, discovery, and utilization of novel neuromorphic materials and device architectures such that the number, timing, magnitude, and interaction modes of electrical pulses processed by neuromorphic elements encode logic and memory functions within a single fabric of dense, energy-efficient computing primitives.[9,15,18] An extensive review of biological neuron characteristics with a focus toward their emulation by complex oxide materials has recently been made available by Park et al.[34] In this work, we focus explicitly on connecting material properties to neuronal and synaptic function and on static/dynamical modulation of transformation characteristics of a canonical metal–insulator transition (MIT) material. To be implemented within neuromorphic architectures, suitable active materials must possess certain requisite material properties to emulate the spiking and plasticity of neuronal systems. Namely, a candidate material must exhibit precisely tuned electronic instabilities, and ideally, offer independent control over 1) magnitude of conductance switching, 2) energy required to induce switching, 3) heat dissipation, 4) switching time, 5) volatility of different states, and 6) the number of accessible internal states. **Figure 1** illustrates several of these transformation characteristics.

1.1. Metal–Insulator Transitions in VO_2

Of the candidates for neuromorphic computing applications, materials wherein Mott physics underpins electronic transitions afford particular promise by dint of their low entropy dissipation and ultrafast transformation dynamics.[7,35–37] VO_2 stands out for its distinctive metal-to-insulator transition occurring at 67 °C.[7,38] The electronic transition in VO_2, which is exquisitely sensitive to the electronic temperature, lies in close proximity to a structural transformation wherein a low-temperature, low-symmetry monoclinic (M1) phase (space group $P2_1/c$) undergoes displacive atomic rearrangement to yield the high-temperature, high-symmetry tetragonal (R) phase (space group $P4_2/mnm$). This transition can be driven nonthermally by photoexcitation,[35] can be modulated to occur under differing state parameters, and can be reversed upon cooling to revert the M1 state. The difference between forward and reverse transition temperatures is the transition hysteresis (Figure 1), which is associated with energy overpotentials needed to nucleate a new phase in either transition direction, and is distinctively sensitive to the microstructure and oxygen stoichiometry.[39–41] While a considerable literature contrasts the Peierls versus Mott origins of the transition in VO_2, a recent dynamical mean field theory model suggests that the transition from the rutile to M1 monoclinic phase in VO_2 is adiabatically linked to a Peierls-type transition but is truly a Mott transition in the presence of intersite exchange.[36] As such, the bandgap of the M1 phase varies as a function of the temperature. A recent neutron scattering study has found that the entropic driving forces for the MIT in VO_2 are underpinned by strongly anharmonic phonons and not electronic contributions. The softer phonons in the high-temperature tetragonal phase drive the increase in entropy that outcompetes orbital-driven stabilization of the insulating phase with increasing temperature. Indeed, phonons account for ≈2/3 of the entropy increase across the MIT.[42]

The MIT brings about a four orders of magnitude discontinuous change in conductivity along with switching of infrared transmittance and thermal conductivity.[43,44] Thus, this transition serves as the basis for off/on (M1/R) high- and low-resistance states of the material. Figure 1 illustrates how transition hysteresis enables retaining off/on states when the material is operated at a temperature falling within the hysteretic range, even after cessation of a transition-driving voltage. This state retention serves as a basis for computational active memory. As will be described in subsequent sections, the MIT hysteresis can be modulated to be narrow or wide by various processing parameters that affect defect dynamics and microstructure, effectively enabling designs for high- or low-volatility in-memory computing.[39–41]

© 2022 Wiley-VCH GmbH
15214095, 2023, 37, Downloaded from https://onlinelibrary.wiley.com/doi/10.1002/adma.202205294 by Texas A&M University Library, Wiley Online Library on [06/12/2023]. See the Terms and Conditions (https://onlinelibrary.wiley.com/terms-and-conditions) on Wiley Online Library for rules of use; OA articles are governed by the applicable Creative Commons License

15214095, 2023, 37, Downloaded from https://onlinelibrary.wiley.com/doi/10.1002/adma.202205294 by Texas A&M University Library, Wiley Online Library on [06/12/2023]. See the Terms and Conditions (https://onlinelibrary.wiley.com/terms-and-conditions) on Wiley Online Library for rules of use; OA articles are governed by the applicable Creative Commons License

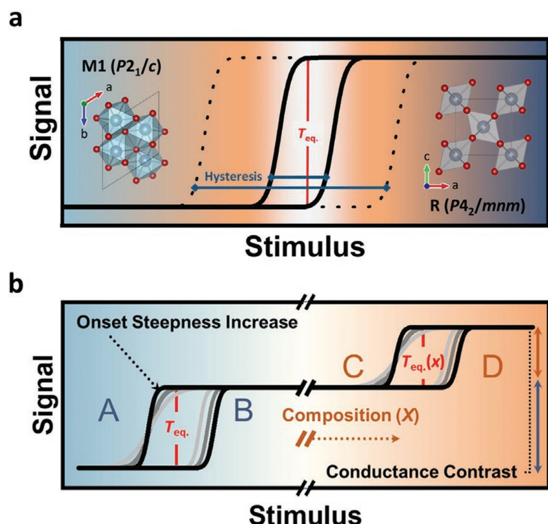

Figure 1. Metal–insulator transition of VO_2. a) The insulating M1-phase of VO_2 reversibly transitions upon stimulation (e.g., by temperature, current, and voltage) to the conductive R-phase of VO_2 with a notable hysteretic gap between properties (i.e., signal: conductance) associated with forward and reverse transitions. Several reports have noted that the electronic transition can be delinked from the structural transformation and engendered with minimal lattice distortion. Widening this hysteresis (dotted line vs solid line) enables greater state stability, serving as a means of embedding low- and high-volatility in-memory computing functions. b) Site-selective modification such as substitutional doping on the vanadium sublattice of VO_2 has the potential to modify a variety of metal-to-insulator properties including $T_{eq.}$, hysteresis width, sharpness of onset, or potentially even drive the system into a new MIT regime by coupling to a dynamical composition field such as oxygen vacancy formation or Li-ion insertion as examples of in-material processing, thereby affording a means of synaptic reconfigurability, which provides a counterpoint to neuronal function obtained with an immutable nonlinear dynamical transition.

1.2. VO_2 in Neuromorphic Computing

In practice, nonlinear dynamical behavior of VO_2 and other neuromorphic materials depend not just on intrinsic material properties but also on the coupling through interfaces to the surrounding matrix and interactions with external circuit elements. Promising work by Yi et al. directed toward the design of neuromorphic circuits utilizing VO_2 emulated distinct electrical signals generated by neurons.[8] These authors replicated 23 distinct neuronal spiking signals including all-or-nothing firing and spike-timing dependent plasticity using simple circuit designs—2 VO_2 memristors and 4–5 passive resistor—capacitor elements which would have required thousands of transistors in conventional CMOS circuitry with potentially lower fidelity of neuronal emulation.[8] In contrast to the Peierls insulator NbO_2 first used in neuristor demonstrations,[30,33] VO_2 can be switched at one-sixth of the energy (<1 fJ spike^{-1}) and at 100× the speed.[8]

The MIT of VO_2 occurs at temperatures slightly lower than the ≈100 °C operating temperatures typical of data servers, within which the VO_2 material would be implemented. By comparison, the majority of materials with high-magnitude conductance switching capability tend to be active at temperatures several hundreds of degrees Celsius above or below room temperature, with a relatively sparse palette of materials that exhibit MITs at the desired operating temperatures.[7] In this article, we first examine the connection between neuromorphic properties and intrinsic material properties through the lens of inverse and forward design. We next review synthetic and processing conditions to modulate VO_2 MIT characteristics encompassing site-selective modification, point defects, strain, particle morphology, and extended defects as a means of systematically tuning neuronal and synaptic function. The various knobs available for tuning transformation characteristics of VO_2 make it a versatile and rich palette for realizing neuromorphic function; however, the strong coupling of spin, charge, atomic, lattice, and orbital degrees of freedom represents a challenge for disentangling transformation characteristics. This strong coupling also makes these systems exceedingly difficult to treat using density functional theory, somewhat limiting the predictive power of first-principles simulations.[36,45–47]

2. Connecting Neuronal and Synaptic Function to Intrinsic Material Properties

A key challenge in the discovery and implementation of neuromorphic materials is the absence of design rules that explicitly map specific neuronal functionality (e.g., thresholding, spike amplification, action potentials, relaxation times) to intrinsic material, interfacial, and circuit properties. This contrasts to Si CMOS, wherein rigorous analytical frameworks unambiguously map device behavior to material properties through benchmarked material compositions and well-defined physical processes that can be accurately described by static functions. Neuromorphic circuit elements exhibit complex and highly nonlinear responses that reflect not just intrinsic material properties but also their coupling with interfaces and interaction with other circuit elements, heat and charge dissipation pathways available within device architectures, and prior conditioning of the input signal and the active element (**Figure 2**). In considering how to elicit a desired set of neuromorphic responses through systematic control of the physics and chemistry of VO_2, it is important to understand its multiphysics and multifield coupling within device architectures that gives rise to specific aspects of neuronal and synaptic function as portrayed in Figure 2.

The ultimate criterion for the utility of a given material for neuromorphic computing is the capability for desired dynamics that emulate action potential spiking, plasticity, and other neuromorphic behaviors.[15] This requires understanding how material properties affect the potential for and qualities of resultant dynamical behavior. As depicted in Figure 2, dynamical behavior depends as much on electrical coupling to external circuit elements as on the material properties of the neuromorphic element itself.[48] Furthermore, the dynamical instabilities associated with negative differential resistance (NDR) and self-oscillation manifest in spontaneous localization of heat and current density within narrow current channels.[49,50] Finally, work to quantitatively understand the design vectors to induce certain classes of dynamical behavior (quasi-periodic, bursting, chaotic) is only nascent. Nevertheless, recent work and recontextualization is beginning to form foundational principles relating material properties to instability and dynamics.[51–54]

© 2022 Wiley-VCH GmbH

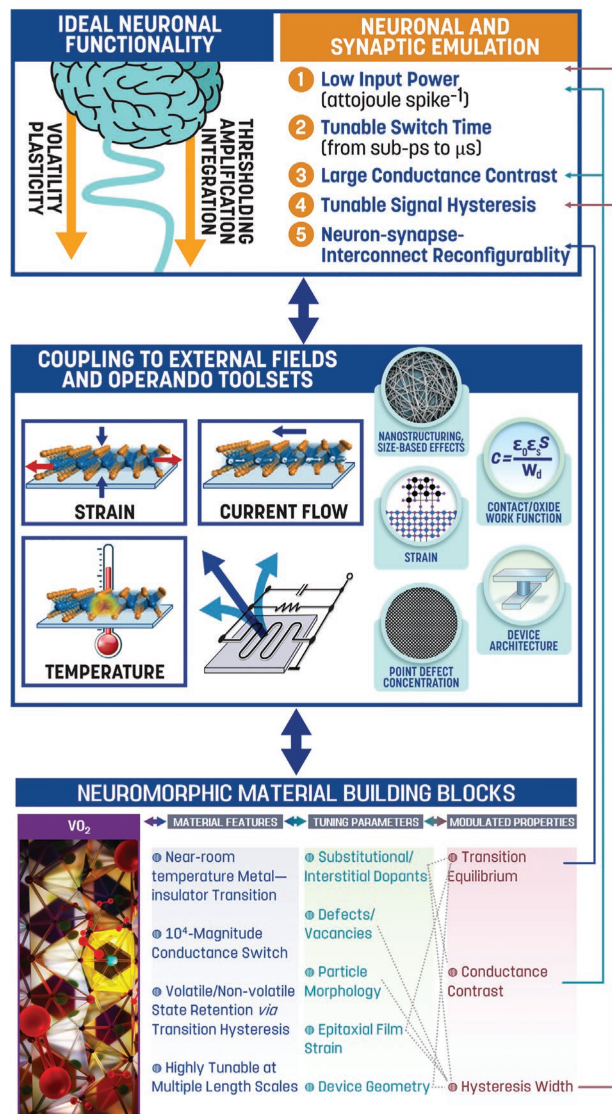

Figure 2. Multiphysics and multiscale modulation of MIT characteristics of VO_2. To create artificial neurons and synapses with tunable functionality from VO_2, the physics and chemistry of nonlinear dynamical electronic transitions need to be understood and controlled not just at the level of intrinsic material properties but with regards to their coupling to external fields across decades of length and time scales. The top panel shows desirable attributes of neuronal and synaptic function; the middle panel illustrates multiphysics and multifield coupling used to modulate neuromorphic response; and the bottom panel shows illustrative compositional, structural, and microstructural levers available to tune material properties. While we map specific dependences, it is worth noting that circuit-level emergent properties represent a complex convolution of material and field coupling parameters.

The key to these principles is a measure of nonlinearity that determines whether the electrothermal properties of a material are sufficiently nonlinear to sustain controlled instability and oscillation. For VO_2 and other thermally activated oxides, especially NbO_2, the electrical and thermal properties are highly temperature-dependent. Together with thermal dynamics governed by Joule power dissipation and Newton's Law of Cooling (NLC)

$$\frac{dT}{dt} = \frac{1}{C}\left(G_{el}(T)\,v^2 - G_{th}(T)(T - T_0)\right) \tag{1}$$

this constitutes these systems as electrothermal memristors,[55,56] and establishes a feedback loop that potentially leads to instability and dynamics.[57,58] Here, T is the temperature of the VO_2 component, t is time, C is the thermal capacitance, v is voltage, T_0 is ambient temperature, and $G_{el}(T)$ and $G_{th}(T)$ are the temperature-dependent electrical and thermal device conductances.

For example, when under a fixed electrical bias, an individual device is driven toward a particular steady-state temperature by the balance of Joule heating and thermal dissipation to the environment (Equation (1)). However, the system never remains at its steady-state temperature for long, since thermal fluctuations are always present.[33] An initial perturbation in temperature changes the electrical and thermal conductance, which in turn modifies the Joule power dissipation. This changes the magnitude and/or sign of subsequent net heating, leading to a new temperature, and so the feedback loop continues (**Figure 3**).

The essential dynamical question is the long-term behavior of this feedback loop: whether the cycle 1) damps itself out, 2) maintains itself, never settling down but never growing without bound, or 3) grows without bound. In case (1) we say the cycle

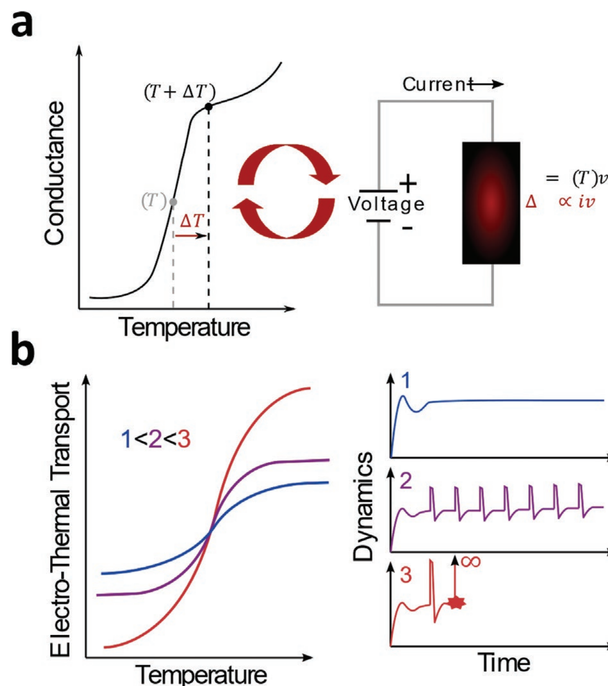

Figure 3. Dynamical electro-thermal instabilities in VO_2. a) Electro-thermal feedback loop that can enable essential neuromorphic dynamics in VO_2. A highly temperature-dependent electrical (and thermal) conductance couples with Joule heating and Newton's Law of Cooling. Feedback is sustained by the ΔT resulting from iv power loss that leads to large changes in conductance G. b) Conceptual relationship between electro-thermal nonlinearity and potential for desired dynamics. A too small nonlinearity (1) results in a rapid damping, rather than a sustained dynamic element; whereas a too large nonlinearity (3) is unstable, but in an undesired, uncontrollable sense. Only (2), nonlinearities that are large enough to be measurable but not so large as to result in uncontrollable instabilities, can lead to sustained neuromorphic dynamics.

© 2022 Wiley-VCH GmbH

15214095, 2023, 37, Downloaded from https://onlinelibrary.wiley.com/doi/10.1002/adma.202205294 by Texas A&M University Library, Wiley Online Library on [06/12/2023]. See the Terms and Conditions (https://onlinelibrary.wiley.com/terms-and-conditions) on Wiley Online Library for rules of use; OA articles are governed by the applicable Creative Commons License

15214095, 2023, 37, Downloaded from https://onlinelibrary.wiley.com/doi/10.1002/adma.202205294 by Texas A&M University Library, Wiley Online Library on [06/12/2023]. See the Terms and Conditions (https://onlinelibrary.wiley.com/terms-and-conditions) on Wiley Online Library for rules of use; OA articles are governed by the applicable Creative Commons License

represents dynamical stability, in the sense that perturbations are self-damping and the system is driven to settle at its steady state. Cases (2) and (3) both represent dynamical instability, although there is an inherent qualitative difference between them, with case (2) representing controllable instability and/or oscillation. From Equation (1), the dynamical properties of the electrical and thermal conductance must play some role in which of the cases (1), (2), or (3) the system settles in. It is this role that is sought to be modulated to enable neuromorphic materials design.

A particularly interesting range of conditions has been labeled edge-of-chaos[59] wherein an external stimulus can drive transformations between self-damping and self-reinforcing regimes. The essential abstraction of the theoretical framework here is the partition of a dynamical system into a smaller internal dynamical "core" and a dissipative external coupling field. For devices based on VO_2 and similar materials, the governing dynamics are Newton's Law of Cooling, which in turn is explicitly dependent on the electrothermal conductance, i.e., the material properties (Equation (1)). A significant recent effort has related the edge-of-chaos behavior to the temperature-dependence of the electrical and thermal conductance of the material.[51] This relation is quantitatively codified in the signs of a pair of defined nonlinearity parameters,[51,57] defined as

$$\Gamma_{\pm}(T) = \left(\frac{G'_{\mathrm{el}}(T)}{G_{\mathrm{el}}(T)} \pm \frac{G'_{\mathrm{th}}(T)}{G_{\mathrm{th}}(T)} \right) (T - T_0) \pm 1 \tag{2}$$

here $\Gamma_{\pm}$ is a generalized nonlinearity parameter, T is the temperature of the VO_2 component, T_0 is ambient temperature, $G_{\mathrm{el}}(T)$ and $G_{\mathrm{th}}(T)$ are respectively the temperature-dependent electrical and thermal device conductances, and $G_{\mathrm{el}}'(T)$ and $G_{\mathrm{th}}'(T)$ are the total temperature derivatives of $G_{\mathrm{el}}(T)$ and $G_{\mathrm{th}}(T)$. When $\Gamma_{-} > 0$, the relative increase in the feed-forward Joule heating term with respect to temperature exceeds that of the feed-back heat dissipation term. This creates the potential for instability. Keeping $\Gamma_{+} > 0$ maintains that the core remains stable; it then requires external coupling for the stability to be controllably lost. This controllable stability loss due to external coupling appears to be key to designing a feedback loop of type (2) that cycles but does not grow without bound. The nonlinearity parameters in terms of the electrothermal properties turn out to be a key to other relevant dynamical questions.[51] VO_2 electrothermal memristors require an external capacitive coupling to lose stability, and the size of the critical capacitance, as well as the resultant self-oscillation frequencies are functions of the nonlinearity parameters. In this way, the electrothermal properties of VO_2 determine its potential for desired neuromorphic dynamics, and can be systematically modulated through the levers noted in the bottom panel of Figure 2 that are discussed in more extensive detail in subsequent sections. The levers denoted here fundamentally modify VO_2 material properties, and thus MIT transformation characteristics. The compact modeling framework described here and extensively elaborated elsewhere,[51] connects key characteristics of neuromorphic circuits such as negative differential resistance, instabilities, oscillations, and bifurcations, to intrinsic material properties through a set of nonlinearity parameters. This approach represents a means of linking circuit-level behavior to specific interventions in materials design. However, while specific dopant/strain/field-coupling influences have become apparent, for instance, doping and control of oxygen stoichiometry to tune the transition temperature and hysteresis width,[60,61] specific linkages spanning from site-selective modification to circuit-level properties remain to be established.

Equation (2) indicates that nonlinearity is essential for neuromorphic behavior. Devices without nonlinear electrothermal conductance functions cannot manifest edge-of-chaos characteristics and externally controllable instability, but devices that fail to be sufficiently nonlinear are also incapable of neuromorphic dynamics. As a simple example (Figure 3B), all else being equal, VO_2 with a smaller conductance contrast and/or less sharp transformation may not be capable of neuromorphic dynamics; whereas VO_2 with a larger switching ratio and sharper transformation may be capable of neuromorphic dynamics, despite the same governing Mott–Peierls physics. However, it is worth noting that it is not true that large switching ratios and sharp transformations should be pursued at any cost: electrical and thermal nonlinearities often coexist and interfere both constructively (Γ_{+}) and destructively (Γ_{-}). For example, if the thermal nonlinearity is large but negative and exceeds the electrical nonlinearity, there will be the potential for instability ($\Gamma_{-} > 0$), but the resultant instability will be uncontrollable ($\Gamma_{+} < 0$), and thus not useful for neuromorphic dynamics. As such, while doping can sometimes suppress the conductance contrast between insulating and metallic states of VO_2, provided the change in conductance is not too small as to cause oscillatory dampening, a few orders of magnitude decrease in conductance contrast between states is still sufficient to manifest neuron-like dynamical behavior in neuromorphic applications.

While the framework reported here has some key limitations such as a simplified view of anhysteretic behavior and lack of full description of temporal variations such as chaotic or bursting signals, it establishes a basis for developing a rigorous process to map specific neuromorphic function to intrinsic material, structural, and interface properties. The ability to incorporate site-selective modifications, local structural perturbations, and control microstructure in VO_2, as well as the ability to systematically tune field coupling, as illustrated in Figure 2, makes it a promising platform for connecting target neuronal and synaptic behavior to the necessary molecular/material properties.

3. VO_2 as a Building Block for Neuromorphic Devices

The choice of VO_2 as a building block for manifesting dynamical oscillations arises from its i) existence of low-entropy transitions across multiple internal states with prospects for reaching the atto-Joule and tens of ps switching required for real-time AI;[8,62,63] ii) potential for tunable multistate conductance switching and reconfigurability (Figure 1) to toggle between neuronal (thresholding, amplification, integration) and synaptic (learning, memory) modes with reconfigurability engineered by coupling to a dynamical composition field such as oxygen vacancy formation or proton/Li-ion insertion;[64–66]

© 2022 Wiley-VCH GmbH

iii) triggering of electronic transition by light, heat, and electric fields; and iv) precision control of properties from atomistic to mesoscale dimensions through numerous finely customizable levers for independent tuning of transformation characteristics, which hold promise for approaching fundamental limits of energy and speed. Furthermore, the transformation characteristics show entirely distinctive modes and strengths of coupling to external composition, strain, thermal, photoexcitation, and electric fields, which provide opportunities of dynamical control of the metal–insulator transition. **Figure 4** schematically illustrates several compositional, structural, and field coupling levers available to tune transformation characteristics. This perspective outlines the assortment of material design levers available to finely tune the intrinsic MIT properties of VO_2 to serve as the active material of which novel neuromorphic computing architectures may be constructed. In this article, we have focused on mechanistic understanding of how these levers control transformation characteristics of VO_2 with an emphasis on illustrative examples instead of attempting a comprehensive account of the extensive literature. We first discuss the role of site-selective modification through dopant incorporation in VO_2 and then review the particular case of thin films with regards to substrate interactions. We discuss the example of electrically driven MITs, which are key to enabling novel neuromorphic computing architectures and then further discuss means of imbuing nonvolatile memory through dynamical modulation of local structure and transformation characteristics. Finally, we discuss photoexcitation-driven phase transformations, mixed optical/electrical functionality, and opportunities for VO_2-based neuromorphic computing beyond energy efficient computing in the design of perceptive systems.

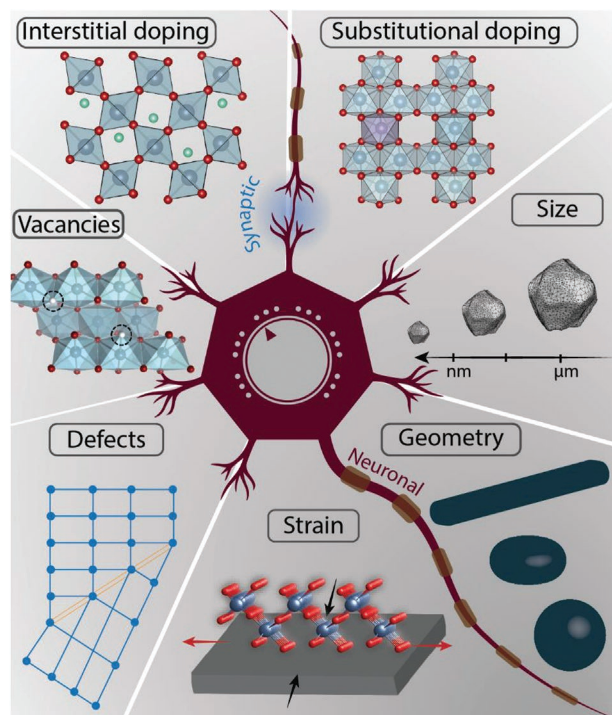

Figure 4. Harnessing VO_2 for neuromorphic computing by modulating its MIT through levers: substitutional and interstitial doping, dimensions and geometry of particles, defects spanning from oxygen vacancies to phase boundaries, and external, epitaxial, and chemical strain.

4. Doping as a Means of Controlling the Metal–Insulator Transition in VO_2

The VO_2 MIT equilibrium temperature ($T_{eq.}$), hysteresis values, and transformation dynamics are governed by the thermodynamics of the phase transformation and kinetic attributes of the phase transformation such as nucleation mechanisms and activation barriers, respectively. Consequently, the MIT characteristics are tunable by modulating phase stabilities, or by hindering, improving, or altogether replacing the primary nucleation mechanism. Site-selective modification of VO_2 through dopant incorporation provides a powerful means of modulating the MIT of VO_2.

We consider first the thermodynamic relationship between the insulating (M1) and the conducting (R) phases of VO_2 in terms of how dopants amend relative phase stabilities with regards to a thermodynamic energy landscape such as illustrated in **Figure 5**A.

On a related note, we then consider the nucleation mechanisms, transformation pathways, and activation energy barriers between minima on the energy landscape with regards to how they are modified by dopant inclusion. Finally, some predictive guidelines for dopant selection are described with regards to neuromorphic function.

4.1. Dopant Effects on Thermodynamic Phase Stabilities

The equilibrium temperature ($T_{eq.}$) of the MIT in VO_2 represents the competition between stabilities of the resultant doped phases (i.e., the M1 or the R phase) to better accommodate changes to the enthalpy and entropy caused by a dopant incorporated within VO_2. Doping differently modifies phase stabilities, as well as the magnitude of structural distortion and change in symmetry across the phase transformation.[67,68] Figure 5C–E illustrates several illustrative cases where the lattice enthalpy and/or conduction entropy contributions to free energy are modified. Typically, changes in the thermodynamic stability of the M1 and R phases upon doping are driven by both a change in the relative lattice enthalpies as well as the electronic entropy. Notably, the free energy is further modified by the strain energy and surface energy, which at the appropriate dimensions are of comparable magnitude to the bulk free energy.[69,70] The difference in free energy for the two phases can be written as

$$\Delta G_{M1\to R} = \left(G_c^{R} - G_c^{M1}\right) + \left(U_{SE}^{R} - U_{SE}^{M1}\right) + \left(U_S^{R} - U_S^{M1}\right) \quad (3)$$

where G_c is the chemical free energy, U_{SE} is the strain energy, and U_S is the surface free energy.[71,72] Local field enhancements as well as surface and strain energy differentials can counteract the chemical free energy terms and stabilize the R phase under conditions of constrained equilibrium (for instance, below a specific particle size or for a certain magnitude and sign of epitaxial strain).

© 2022 Wiley-VCH GmbH
15214095, 2023, 37, Downloaded from https://onlinelibrary.wiley.com/doi/10.1002/adma.202205294 by Texas A&M University Library, Wiley Online Library on [06/12/2023]. See the Terms and Conditions (https://onlinelibrary.wiley.com/terms-and-conditions) on Wiley Online Library for rules of use; OA articles are governed by the applicable Creative Commons License

15214095, 2023, 37, Downloaded from https://onlinelibrary.wiley.com/doi/10.1002/adma.202205294 by Texas A&M University Library, Wiley Online Library on [06/12/2023]. See the Terms and Conditions (https://onlinelibrary.wiley.com/terms-and-conditions) on Wiley Online Library for rules of use; OA articles are governed by the applicable Creative Commons License

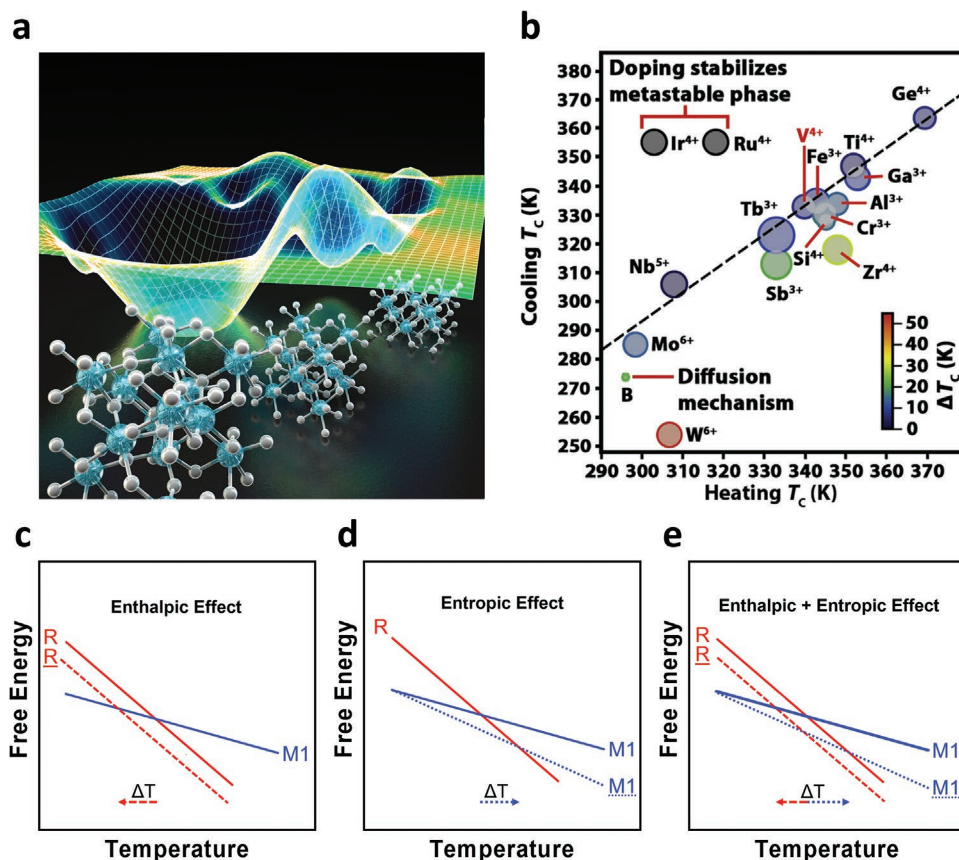

Figure 5. Dopant modulation of thermodynamic energy landscapes. a) Schematic illustration of a free energy landscape with cubic, tetragonal, and monoclinic structures. b) Effect of dopant ion charge and size on the MIT temperatures in VO_2. Dopant ions larger and higher-valent than V^{4+} typically cause decreased MIT temperatures, whereas smaller, lower-valent dopants tend to increase MIT temperatures. Some dopants show a strong propensity to widen the hysteresis of transition (shown in green, yellow, and red). Other dopants (Ir^{4+}, Ru^{4+}) stabilize alternative polymorphs of VO_2. Still yet, other dopants (interstitial boron) imbue dynamical effects on the MIT. b) Reproduced with permission.[7] Copyright 2019, Elsevier. c–e) Modification of free energies of M1 or R phases as a function of dopant incorporation plotted as a dotted line (undoped M1 and R phases are shown as solid lines), illustrating several possible scenarios: c) selective enthalpic stabilization of the R phase depresses the phase transition, d) entropic changes to conductance entropy stabilize the M1 phase as a function of temperature, thereby elevating the phase transition, and e) entropic stabilization of the M1 phase and enthalpic stabilization of the R phase results in an overall depression of the phase transition.

Dopant/alloying elements control transformation behavior by modifying the relative phase stabilities and crystallographic relationships between the two phases principally through 1) introduction of internal chemical strain, 2) influence on electronic band structure, 3) alteration of transformation pathways, and 4) introduction/modification of defect sites and density, which can interact with incipient domains and mobile interphase boundaries.

If the doped M1 phase is made relatively more stable than the doped R phase (such as upon substitutional Ge^{4+} incorporation on the cation lattice),[61,73] then the observed $T_{eq.}$ is increased from the undoped $T_{eq.}$, thus requiring greater energy to initiate the transition from M1 to the R polymorph (**Figure 6**F).[61]

Conversely, if the R phase is made more stable relative to the M1 phase upon doping (such as upon substitutional incorporation of W^{6+} on the cation lattice),[40,75] the $T_{eq.}$ is decreased (Figure 6D). Furthermore, some dopants do not cause shifts in transition characteristics, but instead stabilize altogether different VO_2 polymorphs. Ir-doping for example, has been shown to preferentially stabilize a P-phase VO_2, which does not feature an MIT near room temperature.[76] Dopants such as Al and Cr stabilize an alternative monoclinic phase (M2, space group *C2/m*) that also features an active MIT to the metallic R phase.[77–79] A reversible M2→R substantially elevated transition has been observed at ≈134 °C for Fe-doped VO_2.[80] Interstitial hydrogen incorporation stabilizes two orthorhombic O1 and O2 phases.[81]

The solubility limit of a dopant is the concentration at which the stability contributed by its increased configurational entropy is equal in energy to the instability contributed through increased structural enthalpy. Thus, properties of a dopant such as size and charge with respect to V^{4+} play important roles in determining solubility limits within VO_2. In turn, solubility limits the extent to which a dopant can modulate MIT properties.

The variable valence of vanadium and diverse connectivity of vanadium-centered tetrahedra, square pyramids, and octahedra results in a "rugged" energy landscape characterized by a rich diversity of metastable polymorphs.[72] The synthetic design space for stabilization of VO_2 is complex and limited to

© 2022 Wiley-VCH GmbH

15214095, 2023, 37, Downloaded from https://onlinelibrary.wiley.com/doi/10.1002/adma.202205294 by Texas A&M University Library, Wiley Online Library on [06/12/2023]. See the Terms and Conditions (https://onlinelibrary.wiley.com/terms-and-conditions) on Wiley Online Library for rules of use; OA articles are governed by the applicable Creative Commons License

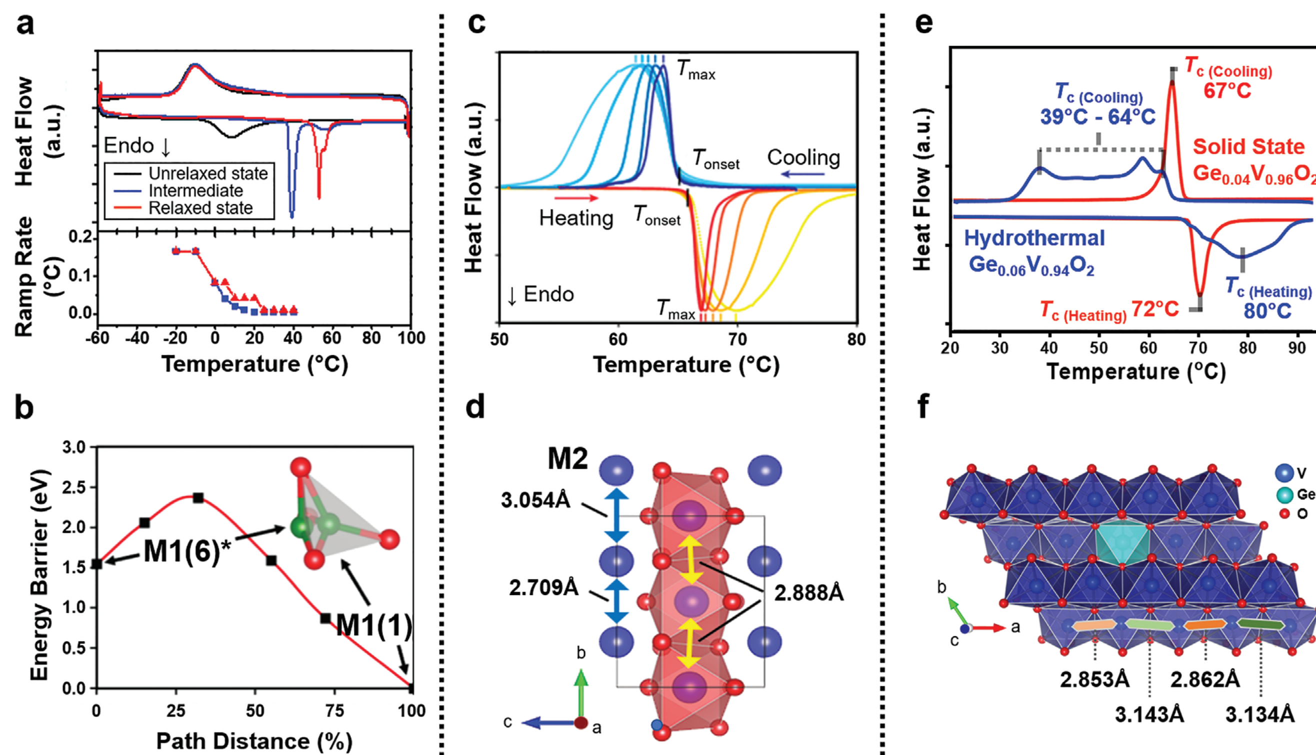

Figure 6. Dopant influences on the structure of VO_2 and MIT transformation characteristics. a) Dynamical, time-dependent forward transitions are observed in interstitially boron-doped VO_2. b) Upon cooling into M1 VO_2, boron atoms reside in a metastable trigonally coordinated site; over the period of several hours, boron migrates into its most stable, tetrahedrally coordinated site. a,b) Reproduced with permission.[74] Copyright 2020, American Chemical Society. c) Substitutional incorporation of (hexavalent) tungsten in VO_2 asymmetrically depresses $T_{eq.}$, with further depression achieved in the reverse (cooling) transition. d) *W* doping induces anisotropic stress gradients that stabilize extended M2 VO_2 domains. c,d) Adapted with permission.[40] Copyright 2018, American Chemical Society. e) Substitutionally doped germanium raises $T_{eq.}$ and disfavors formation of oxygen vacancies; exploiting oxygen-rich or oxygen-poor synthesis conditions facilitates widened or narrowed hysteresis, respectively. f) Doping Ge into VO_2 effectuates increased V–V dimerization, stabilizing the M1 phase and consequently raising the $T_{eq.}$ e,f) Adapted with permission.[61] Copyright 2022, Royal Society of Chemistry.

a narrow range of oxygen stoichiometries. Figure S1A of the Supporting Information plots the Ellingham diagram of V–O compounds, which illustrates narrow sliver of oxygen stoichiometries where VO_2 is stabilized,[82] which in turn necessitates careful control of oxygen partial pressure in physical vapor deposition processes.[83,84] Similarly, solution-phase synthesis requires careful control of the Pourbaix diagram with regards to temperature, pH, and the redox potential in order to speciate precursors to VO_2 (Figure S1B, Supporting Information).[85,86] In hydrothermal synthesis, this is commonly achieved through judicious choice of the reducing agent and pH conditions.[85] The manner of a dopant's incorporation is an important factor with repercussions both for configurational entropy and lattice strain. The extent of incorporation is given by $[X] = p(\alpha, \beta, \gamma, \ldots)$, where p describes the concentration of incorporated element X, as a function of processing variables ($\alpha, \beta, \gamma, \ldots$). This "incorporation function" has been found to be highly nonlinearly dependent on different process variables, such as temperature, pH, precursor concentration, etc.,[38,87,88] governed in solution-phase synthesis by the complex Pourbaix diagram of vanadium oxides alloyed with other cations.

The literature most often recounts cationic substitutional doping, in which the dopant inhabits a site otherwise filled by vanadium cations of the host undoped VO_2 lattice. Cationic substitutional dopants of smaller radii or lesser charge than the V^{4+} ion generally tend to shift the $T_{eq.}$ up, whereas larger cations and greater oxidation numbers generally tend to cause the MIT to shift to lower temperatures as shown in a collated representation mined from the literature in Figure 5B.[7,40,61,73,89–96]

Substitutional dopants have mostly been incorporated on the cation lattice rather than the anion sublattice, although F-doped sublattice substitutions have been reported to decrease $T_{eq.}$.[97,98] By contrast, interstitial dopants reside in holes within the host VO_2 lattice. Interstitial dopants tend to be small such as H, Li, B, and Na, and also tend to decrease $T_{eq.}$.[74,87,99,100] It is typical for a dopant to exclusively incorporate in a site-selective manner either substitutionally or interstitially in the manner which best reduces strain in the VO_2 lattice, although N-doping is a noted exception where energetic preferences for doping on the anion sublattice and interstitial occupancy are comparable.[101]

The importance of the coordination environment surrounding a dopant atom on $T_{eq.}$ is readily demonstrated by interstitially B-doped VO_2, which manifests a dynamical MIT with a response dependent on the duration of time for which the material has rested in its pretransitioning state.[74] Beginning with the R phase, the reverse transition to the M1 phase initially relocates the B atoms in a metastable, trigonally coordinated site (Figure 6B).

Over several hours the B atoms eventually relax into a thermodynamically preferred, tetrahedrally coordinated site. This

 © 2022 Wiley-VCH GmbH

is manifested by different $T_{eq.}$ values depending on how long the B_xVO_2 was allowed to relax after the initial transition—with little time to relax (and B atoms situated in higher energy, metastable sites), the observed $T_{eq.}$ is higher than when the B_xVO_2 is allowed to fully relax over several hours or days (Figure 6B). The thermally activated B migration thus provides a means of defining an atomic hourglass and thermometer that couples with the dynamical MIT of VO_2.

4.2. Dopant-Modulation of Nucleation Mechanisms and Transformation Kinetics

To launch a solid–solid symmetry-raising Martensitic transformation, a transformation dislocation needs to be nucleated and propagated across the material.[71,102] The phase transition in VO_2 is initiated by local undimerization of V–V pairs; an ensemble of dilated V–V pairs ultimately transform into a shear wave that propagates across the lattice near the speed of sound.[35,103] The hysteresis of the MIT results from an energetic overpotential arising from the availability (or lack thereof) of potent nucleation sites. Potent nucleation sites may come in a variety of forms including but not limited to point defects like dopant sites and atom vacancies or line defects such as twinned planes. Consequently, defects serve as potent nucleation sites during the VO_2 metal-to-insulator transition because less driving force is required to nucleate the already locally unstable defect into the new phase.

Although both the forward (M1→R) and reverse (R→M1) transitions occur at temperatures governed by the relative thermodynamic phase stabilities as altered by site-selective modification (Figure 5), the forward transformation from a lower-symmetry M1 phase to a higher symmetry R phase is readily nucleated at twin planes, whereas the nucleation limitations are more pronounced for the reverse transition. Consequently, the effects of a dopant on the transition hysteresis can be asymmetric by modulating the forward and reverse transition monotonically yet disproportionately as a consequence of altering nucleation factors. In several cases, aliovalent substitution on the vanadium lattice with higher oxidation state cations strongly suppresses oxygen vacancy formation, which then results in a substantially increased nucleation barrier and the need for overcooling, which is manifested in the form of increased hysteresis.[40,60,61,104] By contrast, incorporating substitutional cationic dopant ions larger in size and lower in charge than V^{4+} (such as Sb^{3+}) tend to result in increased oxygen vacancies.[96] As another illustrative example, ab initio calculations indicate bivalent Mg^{2+} substitutional doping induces oxygen vacancies as a primary means of charge compensation.[105] Increasing defect concentration in VO_2 frequently results in a narrower MIT hysteresis width. Indeed, this effect is notably pronounced for increasing concentrations of doped Ti and Au.[89,106–108] Dopants are themselves point defects as a result of distortions induced by the impurity ion, which generate a point of local instability compared to the undoped, pristine lattice.[104,109] Conversely, the higher the crystalline quality of VO_2, the wider the hysteresis. Indeed, at reduced dimensions, where defects are readily healed through migration to surfaces, the hysteresis between heating and cooling transitions can span several tens of degrees.[110,111] When nucleation constraints are removed, the hysteresis depends solely on the lattice incompatibility between the transformed and parent phases.

We have recently demonstrated that substitutional dopant incorporation and oxygen stoichiometry can be used to decouple modulation of transformation temperature and hysteresis (Figure 6E).[61] We found that the substitutional inclusion of Ge increases the energetic cost to form oxygen vacancies in VO_2.[61] This dopant effect in tandem with preparation in oxygen-rich synthesis conditions enables a broad hysteresis extending well below the undoped VO_2 transition temperature, despite the thermodynamic influence of Ge^{4+} monotonically raising $T_{eq.}$.[61,73] The depletion of oxygen vacancies to serve as nucleation sites in this system implies that a substantial degree of undercooling is needed to nucleate and propagate the reverse transition. By preparing Ge-doped VO_2 in oxygen-poor synthesis conditions (more likely to possess oxygen vacancies), a starkly narrower hysteresis was obtained.

In notable cases, introduction of a dopant results in formation of defects with longer ranges of order that may instead serve as nucleation sites. In substitutionally tungsten-doped VO_2, the presence of W induces anisotropic strain sufficient to nucleate local M2 domains (Figure 6C,D), the extended phase boundaries of which serve (along with twin-planes) as the preferred nucleation sites of the forward transition.[40,112]

4.3. Considerations in Doping of VO_2 for Neuromorphic Computing

Materials design ideas can start to be connected to the specific needs of neuromorphic architectures. Neuromorphic computing elements made from VO_2 will likely need to operate near the ≈80–100 °C operating temperatures typical of data servers. With a $T_{eq.}$ near 67 °C, undoped VO_2 will require modification to raise its $T_{eq.}$ by several decades. Small, substitutional dopants with tetravalent-or-lower oxidation states are preferable to permanently increase the $T_{eq.}$ Cr^{3+} elevates the MIT to nearly 100 °C at sufficiently high concentrations;[113] Fe^{3+} doping similarly stabilizes the M2 phase and elevates the transition temperature as high as 134 °C as a result of segregation of iron atoms to V2 zigzag chains.[80] Ge^{4+} is a promising candidate dopant because it has been shown capable of elevating $T_{eq.}$ over 90 °C in films,[73] and its hysteresis can be modulated depending on synthesis conditions.[61] The latter important factor active memory must be colocated with processing in neuromorphic computing materials, and there is need both for easily overwritten, as well as easily retained, memory (Figure 1). The inverse design approach outlined in Section 2 establishes a theoretical basis for linking material properties to neuromorphic circuit behavior by combining compact modeling with mechanistic understanding of how dopants tune specific transformation characteristics[51] but needs further elaboration to obtain more deterministic control of circuit behavior.

Alternative arrangements for high- and low-volatile memory complements might involve selecting a pair of dopants. Generally speaking, the effect of concentration of dopants X and Y, on property M will follow some functional (nonlinear) relationships

© 2022 Wiley-VCH GmbH
15214095, 2023, 37, Downloaded from https://onlinelibrary.wiley.com/doi/10.1002/adma.202205294 by Texas A&M University Library, Wiley Online Library on [06/12/2023]. See the Terms and Conditions (https://onlinelibrary.wiley.com/terms-and-conditions) on Wiley Online Library for rules of use; OA articles are governed by the applicable Creative Commons License

$$M = f([X]/[X_0]),\ M = g([Y]/[Y_0]) \tag{4}$$

where $[X_0]$ and $[Y_0]$ are reference concentrations that serve to normalize the relative effectiveness of different dopants. Considering a system with two (or more) dopants, the function

$$MM = h([X]/[X_0],[Y]/[Y_0]) \tag{5}$$

represents the observed bivariate dependence of property M, leading to a readily defined interaction term

$$\eta([X]/[X_0],[Y]/[Y_0]) = h/(f+g) \tag{6}$$

where $\eta > 1$ for concentrations where dopants interact cooperatively, or $\eta < 1$ for where they interact destructively. A similar approach could be extrapolated to multivariate doping scenarios.

Three scenarios can be envisioned. a) Dopants which tend to have the same effect on a property but as a result of different mechanisms (e.g., homovalent substitutional elements which result in lattice-strain based stabilization of a high-temperature phase, and aliovalent equidimensional substitutional elements which principally serve to alter the electronic structure, but with the same resulting effect). This may enable magnification of a particular material property beyond the solubility limit of a single dopant. b) Dopants which occupy distinct positions in the lattice (e.g., interstitial vs substitutional), but tend to have similar functional outcomes (e.g., depressing a critical transition temperature, $T_{eq.}$). c) Dopants which compensate each other in some aspect (e.g., a larger and a smaller substitutional atom, which could cluster and result in minimal net lattice deformation), while still introducing a new functionality (e.g., a potent defect site for nucleation, which could potentially modify transformation kinetics without degrading crystallinity or substantially modifying the transition temperature).

It is likely that an optimally doped VO_2 for neuromorphic purposes will be doped by more than one dopant species. Codoping offers a means of synergy in modulation of the VO_2 MIT, and indeed offers a vast design space that has only just started to be explored. In Sr-/W-substitutionally codoped VO_2 for example, W^{6+} was effective in significantly decreasing $T_{eq.}$, whereas Sr was used to increase the material bandgap to suit application needs.[114] In a Nb-/Cr-codoped VO_2, the dopants have antagonistic effects as envisioned in the third scenario—the transition hysteresis is almost entirely eliminated, whereas unwanted $T_{eq.}$ shifts are ameliorated by selecting dopants with counteracting decreasing (Nb^{5+}) and increasing (Cr^{3+}) effects on $T_{eq.}$.[107,115] A preliminary basis for charge carrier engineering while simultaneously shifting $T_{eq.}$ through codoping strategies has been demonstrated in Mg-/Fe-codoped VO_2.[116]

4.4. Toward Generalizable Design Principles for Modulating the MIT in VO_2

A great diversity of elements has been incorporated in VO_2, including cationic and anionic substitutional dopants in addition to interstitial dopants. General trends emerge throughout the literature that smaller substitutional cations with lower-or-equal valence with respect to V^{4+} raise MIT transition temperatures, whereas the opposite effect is true for larger cationic dopants of higher valence. A phenomenological Landau model developed by Shi and Chen predicts the following general form for modification of the transition temperature[117]

$$T_0 \rightarrow T_0 - \frac{T_{eq.}\left[\Theta_1\left(R_d^3 - R_{V^{4+}}^3\right)/R_{V^{4+}}^3 + \Theta_2\left(\upsilon_d - \upsilon_{V^{4+}}\right)\right]x}{a} \tag{7}$$

where $T_{eq.}$ is the undoped metal–insulator transition temperature (338 K), T_0 is the "Curie–Weiss temperature" corresponding to structural order, Θ_1 and Θ_2 are coupling constants, R_d is the radius of the dopant ion, $R_{V^{4+}}$ represents the radius of V^{4+} ions, x is the atomic fraction of the dopant with respect to vanadium, υ_d is the valence of the dopant ion, $\upsilon_{V^{4+}}$ is the formal valence of vanadium (4+), and a is a constant pertaining to symmetry relations during the lattice transformation.[117,118]

Dopants that provide novel nucleation sites or affect oxygen vacancies tend to have profound effects on the transition hysteresis. The transition hysteresis governs the on/off (R-phase/M1-phase) state retention upon removal of the excitation. This serves as a basis of memory within the same material to also be used for logic operations during computation. If nucleation constraints are alleviated, geometric compatibility of transformed and parent phases dominates hysteresis width as per the nonlinear theory of Martensitic transitions.[41] Identification of dopants that reduce the symmetry variation across the phase transformation such as through control of the middle eigenvalue and cofactors of the transformation stretch tensor hold promise for systematic control of hysteresis.[41,67] Conversely, approaches to imbue nonvolatile memory storage to the MIT in VO_2 are discussed in Section 6.5. Finally, thoughtful selection in codopant pairs has just started to be explored but demonstrates fine control over MIT parameters and material properties through balancing of lattice distortions and charge compensation mechanisms.

The interplay of material processing parameters and their effect on transformation characteristics is complex, and often requires careful attention to reach optimal balances between multiple defect features. For example, we have recently achieved a delicate balance between W-doping concentration, particle size, and particle crystallinity (the last being related to the conductance differential between insulating and conductive phases).[119] Through judicious selection of thermal annealing parameters to alleviate dopant exsolvation and encapsulation with a passivating layer to allow annealing-induced enhancements in crystallinity, we have achieved W-alloyed VO_2 with a depressed phase transformation temperature but large magnitude of the phase transformation.[119] Modulation of VO_2 by doping, stress, and other processing parameters brings critical material properties within range of predetermined operating conditions while simultaneously altering material performance at those operating conditions.

For application of modified VO_2 materials in neuromorphic computing, the following conclusions can be derived. First, active systems tend to operate at elevated temperatures, so it is advisable to include a dopant that will increase the $T_{eq.}$ of the MIT. Dopant solubility limits should be kept in mind,

© 2022 Wiley-VCH GmbH

15214095, 2023, 37, Downloaded from https://onlinelibrary.wiley.com/doi/10.1002/adma.202205294 by Texas A&M University Library, Wiley Online Library on [06/12/2023]. See the Terms and Conditions (https://onlinelibrary.wiley.com/terms-and-conditions) on Wiley Online Library for rules of use; OA articles are governed by the applicable Creative Commons License

15214095, 2023, 37, Downloaded from https://onlinelibrary.wiley.com/doi/10.1002/adma.202205294 by Texas A&M University Library, Wiley Online Library on [06/12/2023]. See the Terms and Conditions (https://onlinelibrary.wiley.com/terms-and-conditions) on Wiley Online Library for rules of use; OA articles are governed by the applicable Creative Commons License

when possible, to ensure the VO_2 system may be doped at concentrations sufficient to bring the $T_{eq.}$ in range of the desired operating temperature. Codoping represents a potential way to push above and beyond limits of singular dopants. Next, the hysteresis of the MIT is a useful feature to exploit for neuromorphic materials so as to provide a selection of volatile or less-volatile memory capabilities. Finally, although codoping in VO_2 remains largely underexplored, combining multiple, disparate dopant effects enables materials design and MIT engineering possibilities extending beyond the scope of individually doped systems.

5. Thin Films of VO_2 and Their Potential for Applications in Neuromorphic Computing

Thin films of VO_2 are of particular relevance due to the scalability of fabrication processes based on lithography techniques and compatibility with foundry capabilities. Several reviews have examined the deposition of high-quality VO_2 thin films[120,121] and the resulting processing–microstructure–property relationships.[122,123] Here, we will focus instead on reviewing methods for controlling the MIT of VO_2 thin films using epitaxial strain, use of dopant incorporation, and the use of high-energy irradiation to control defect populations, and as well as the intersections between these areas (Figure 4). These approaches are keys to developing systems with deterministic control over transformation characteristics, as well as in realizing systems with long operational lifetimes that are required in computing applications (e.g., endurance beyond 10^9 cycles). Achieving these goals requires establishing the intrinsic mechanical properties of the thin films, the stress evolution behavior of the films during phase transformations, and design strategies to design damage-free operation of VO_2-based neuromorphic device elements.

MIT behavior of VO_2 thin films is tied to film geometry and the corresponding boundary conditions. In undoped freestanding particles, the transformation has been observed as abrupt with no phase coexistence regime,[39,124,125] consistent with a nucleation-limited transition. Additionally, particle size leads to different transformation temperatures with larger particles having more nucleation sites and thus faster switching.[104,119,126] By contrast, mechanically constrained VO_2 shows rich phase coexistence characteristics, resulting from local thermoelastic equilibrium (**Figure 7**). For instance, formation of periodic and dynamically tunable nanodomains in constrained nanobeams has been attributed to the competition between elastic strain energy (from lattice mismatch) and domain wall interfacial energies.[124,125,127] Nanometer-sized domains are similarly stabilized in thin films but tend to be disordered without long-range periodic organization.[128]

5.1. Lattice Strain in VO_2 Nanobeams and Thin Films

Applying uniaxial tensile stress along the c_R-axis modifies the bonds lengths of V–V bonds and can affect the $T_{eq.}$ by impeding V–V dimerization. This is perhaps most clearly discernible upon application of external strain to nanobeams along specific crystallographic axes. Experiments examining the application of external strains have revealed the emergence of metastable M2 and T phases, which are stabilized under anisotropic strain (Figure 7A). These polymorphs exhibit parallel transformation pathways to the rutile phase upon heating. Park et al. strained VO_2 nanobeams to construct a stress–temperature phase diagram and found a triple point at which multiple phases are degenerate (Figure 7A).[129] Cao et al. found that applying strain to clamped nanobeams induces phase inhomogeneity; periodic triangular domains are formed along the length of the nanobeams to relax strain and minimize interfacial energies (Figure 7B).[124] The distinctive strain sensitivity of VO_2 is particularly strong along the c_R-axis, which controls the closing of the bandgap, as has been seen in cluster-dynamic mean field theory calculations.[130] A detailed perspective of DFT and

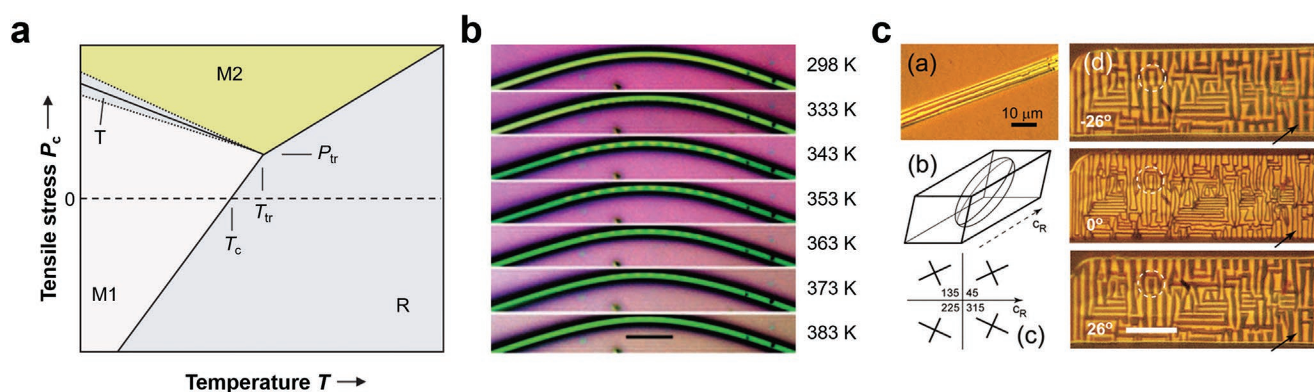

Figure 7. Strain modulation of the VO_2 phase diagram. a) Strain manifests in the VO_2 system by stabilizing one phase relative to each other. b,c) Phase coexistence resulting from local thermoelastic equilibrium. a) Stress–temperature phase diagram of VO_2 resulting from tensile strain. Here T_c indicates unstressed $T_{eq.}$, P_{tr}, and T_{tr} indicate the pressure and temperature associated with the triple-point of M1, M2, and R-phases of VO_2, and T indicates the triclinic T-phase VO_2 structure. b) Optical images of a VO_2 nanobeam heated through the transformation during application of external bending strain, resulting in coexistence of domains in local thermoelastic equilibrium. c) Textured microstructure comprising R- and M1 phases that results from transformation of a single-crystal VO_2 nanobeam that is elastically coupled to the substrate. a) Reproduced with permission.[129] Copyright 2013, Springer Nature. b) Reproduced with permission.[124] Copyright 2019, Springer Nature. c) Reproduced with permission.[79] Copyright 2010, American Chemical Society.

 © 2022 Wiley-VCH GmbH

15214095, 2023, 37, Downloaded from https://onlinelibrary.wiley.com/doi/10.1002/adma.202205294 by Texas A&M University Library, Wiley Online Library on [06/12/2023]. See the Terms and Conditions (https://onlinelibrary.wiley.com/terms-and-conditions) on Wiley Online Library for rules of use; OA articles are governed by the applicable Creative Commons License

beyond-DFT calculation methods used to identify and investigate electron-correlated metal oxides for neuromorphic computing is available elsewhere.[34]

In contrast to nanobeams, stresses in epitaxial films are typically biaxial in nature, as they originate from in-plane lattice mismatch between the film and the underlying substrate. In films under biaxial stress, the stress–temperature phase diagram is modified because of the lattice mismatch, which depends on the underlying substrate. For VO_2 on TiO_2 (001), both the a_R-and b_R-axes are equally strained; tension along the c_R-axis raises the temperature of the MIT, as observed in phase diagrams constructed by Park et al.[129] and experiments by Muraoka and Hiroi.[131] Hard X-ray photoemission spectroscopy studies of buried interfaces of VO_2 thin films on TiO_2 (100) confirm that strain along the c_R-axis stabilizes the M2 phase but at a different temperature than the proposed phase diagram as a result of strain-induced increased electron correlation, which in essence triggers an orbital-selective Mott transition.[132] Aetukuri et al. used a buffer layer of RuO_2 with varying thicknesses to apply tension along the c_R-axis and in-plane compression along the a_R-axis, and found that the MIT shift is correlated with the d|| orbital occupancy of the metallic R state.[133] Selective modulation of the V–V bond length through anisotropic strain allows for continuous tuning of the orbital filling of V 3d hybrid states oriented along the c_R-axis, enabling precise modulation of $T_{eq.}$.

M2 and T polymorphs are stabilized under anisotropic strain with partial undimerization of V–V chains, thus serving as a means of strain minimization. Unlike in nanobeams, it has been found that biaxial strain can lead to phase coexistence in a more random and percolative manner for epitaxial VO_2 thin films on Al_2O_3 ($\bar{1}$012), TiO_2 (110), and Al_2O_3(0001).[134–136]

Applied strain through epitaxial mismatch has been realized with several different substrates such as the *c*-, *m*-, and *r*-cuts of Al_2O_3,[135,137,138] various cuts of $(TiO_2)_R$,[131,136,139–142] and implementation of buffer layers such as $(TiO_2)_R$, Al_2O_3, NiO, and SnO_2.[143–147] A collated summary of the role of epitaxial mismatch in modulating the MIT in VO_2 excerpting a substantial span of the relevant literature is provided in **Figure 8**b. $T_{eq.}$ for VO_2 scales linearly with the strain along the c_R-axis on TiO_2 substrates. With decreasing thickness, indicated by various shades of purple in Figure 8, the interface between the film and the substrate becomes more relevant as strain is not as relaxed. In TiO_2 (001), with a layer of ≈7 nm of VO_2, it has been documented that the transformation does not occur; even at high temperatures, the film remains insulating as a result of interdiffusion of titanium atoms, which gives rise to the formation of a new $(V,Ti)O_2$ solid solution.[70,148]

Related to these observations, the competition between the domain interfacial energy and the elastic lattice misfit energy has received considerable attention since it governs the dimensions and periodicity of phase separation (**Figure 9**).[136,149–152] A bulk single crystal of VO_2 displayed a sharp metal–insulator interface, whereas a polycrystalline VO_2/r-sapphire system showed formation of a complex percolative network of domains across the phase transformation; the greater phase heterogeneity of the latter stems from several in-plane orientations (a_M-axis) existing in polycrystalline systems as compared to the singular orientation of single-crystalline VO_2 films.[150,151] Consistent with this idea, polycrystalline VO_2 thin films grown on *c*-axis sapphire transform to the R-phase through a series of independent nucleation events; the distribution of local strains is accumulated at the domain boundaries of VO_2 upon thermal cycling and brings about a monotonic increase of the transition temperature and decrease of the hysteresis.[135] VO_2/TiO_2 $(110)_R$ yields a stripe-like pattern of VO_2 polymorphs as a result of lattice mismatch along $[110]_R$ and $[001]_R$ (Figure 9);

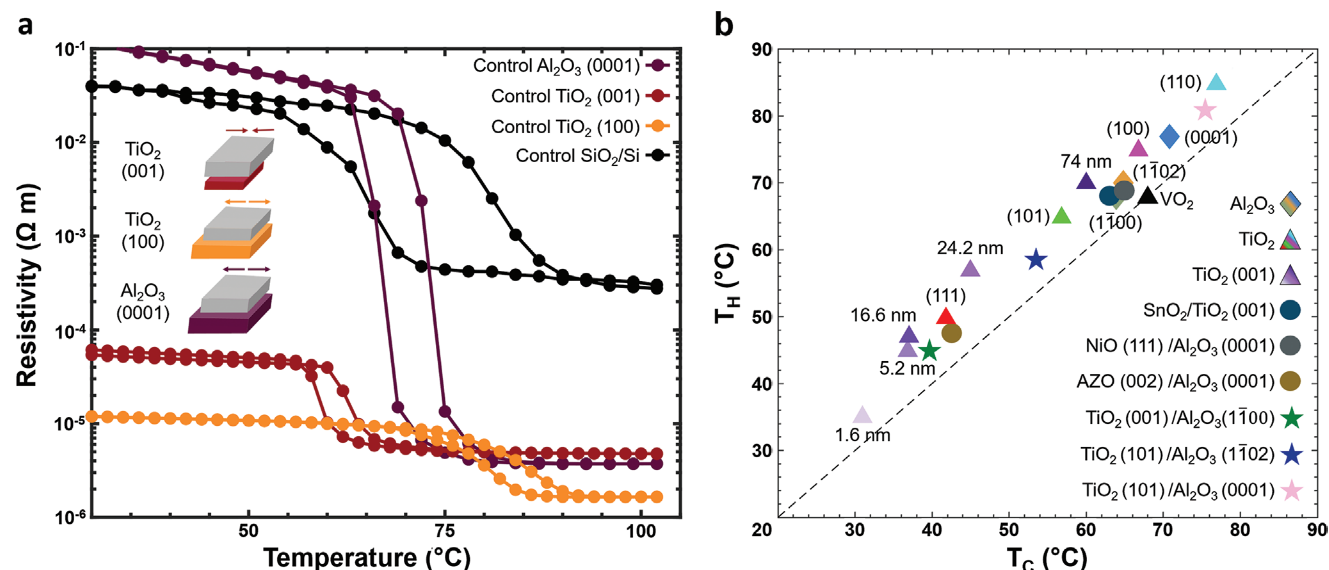

Figure 8. Substrate effects on MIT characteristics of VO_2 thin films. Thin films grown on rigid solid substrates invariably result in elastic interactions between the film and the underlying substrate. When there is an epitaxial crystallographic relationship between the film and the substrate, this result in additional anisotropic lattice strain which can stabilize one phase with respective to the other, as demonstrated by a) thermal transformation curves on different epitaxially grown films.[131,135–147] b) MIT in VO_2 films grown on different substrates are impacted by 1) the crystal structure of the underlying substrate, 2) the thickness of the overlying VO_2 film, and 3) the existence of a buffer layer.

 © 2022 Wiley-VCH GmbH

15214095, 2023, 37, Downloaded from https://onlinelibrary.wiley.com/doi/10.1002/adma.202205294 by Texas A&M University Library, Wiley Online Library on [06/12/2023]. See the Terms and Conditions (https://onlinelibrary.wiley.com/terms-and-conditions) on Wiley Online Library for rules of use; OA articles are governed by the applicable Creative Commons License

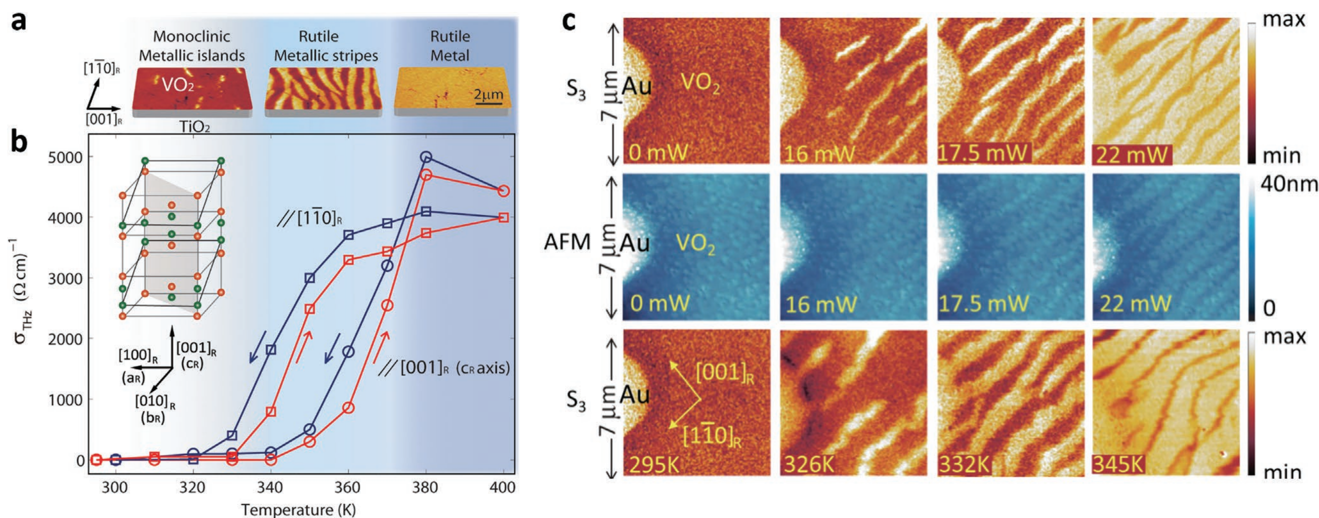

Figure 9. Imaging the MIT in VO_2 thin films. a) Near-field IR images showing the three stages of the MIT. b) Anisotropy along the $[1\bar{1}0]_R$ and $[001]_R$ directions using temperature-dependent THz conductivity (σ_{THz}). c) Infrared near field (S_3) and AFM images of a VO_2 film at different temperatures. Adapted with permission.[136] Copyright 2013, American Physical Society.

the periodic organization of the phase domains reflects the balance between minimization of lateral lattice coherency strains and interfacial lattice mismatch.[136,151] By contrast, highly oriented VO_2/TiO_2 $(001)_R$ with the c_R-axis as the out-of-plane direction shows a gradual and continuous phase transformation pattern.[150]

5.2. Alloying of VO_2 Thin Films

As discussed in preceding sections, dopants induce local structural distortions, trigger electron or hole injection, and modify defect distributions. Successful early attempts at thin film doping included incorporation of tungsten and molybdenum with depressed $T_{eq.}$ values of 40 and 55 °C, respectively.[153] Later works with the same dopants established a linear relationship between the $T_{eq.}$ and $x \leq 0.020$ in $V_{1-x}(Mo/W)_xO_2$.[154,155] By contrast, doping of titanium in amounts from 5 to 20 at% leads to a smeared transformation ranging from 75 to 80 °C.[106] Dopant incorporation has been achieved through kinetic control using methods such as sputtering, sol–gel processing, or chemical vapor deposition, wherein the kinetics of crystallization exceed kinetics of dopant diffusion and exsolvation.[119] Alternatively, a few studies have implemented postsynthetic dopant incorporation through methods such as ion implantation.[156] Substitutional aliovalent dopants such as W^{6+}, Mo^{5+},[154,157] and Nb^{5+},[158] with higher valence and larger radii than tetravalent vanadium shift $T_{eq.}$ to lower temperatures. Tungsten incorporation brings about a depression of $T_{eq.}$ at ≈43–55 °C at%$^{-1}$ W^{-1}.[158–160] Smaller ions that induce a relatively modest lattice distortion such as F^- incorporated on the anion lattice and H^+ incorporated in interstitial sites tend to have a less pronounced effect on the transition temperature.[161,162] Substitutional incorporation of formally tetravalent and lower valence cations such as Ge^{4+},[73,163] Ti^{4+},[106,164] Al^{3+},[165] and Cr^{3+} tend to increase $T_{eq.}$; a $T_{eq.}$ of ≈100 °C has been observed for $V_{0.8}Cr_{0.2}O_2$ prepared by pulsed laser deposition on Al_2O_3 (0001).[113]

5.3. The Intersection of Strain and Chemical Alloying

Incorporation of dopants in VO_2 thin films clearly modifies the MIT; however, differences in the effects of site-selective modification between epitaxial and doped films are less explored. A question of particular importance is the extent to which strain from dopants (chemical strain or pressure) couples with epitaxial strain derived from lattice mismatch with the substrate? Epitaxial $V_{0.97}W_{0.03}O_2$ deposited on *a*-plane (110) sapphire had a reduction in $T_{eq.}$ of 23 °C at%$^{-1}$ W^{-1} and exhibited an MIT with decreased sharpness.[166] Use of reciprocal space mapping in a tungsten-doped VO_2/TiO_2 (001) system confirmed the tension on the *c*-axis arising from the larger size of tungsten.[167] Furthermore, the concentration of tungsten (x in $W_xV_{1-x}O_2$) systematically reduces the $T_{eq.}$ at concentrations $x > 0.07$. Concentrations between $0.07 \leq x \leq 0.095$ undergo a dramatic decrease in resistivity with slight upturns, which indicates the formation of a metallic matrix with the presence of insulating puddles. Further increase in dopant concentration beyond this point leads to an increase of $T_{eq.}$ and a smearing of the transformation at points $x > 0.20$. The shift to higher temperatures with doping concentrations and its relation to strain coupling remains an opportunity for future investigations. Doping with Cr and Nb in VO_2 on Al_2O_3 (0001) results in the reduction of the thermal coefficient of resistance and the $T_{eq.}$ through lattice deformation. The full scope of correlations between substrate strain and dopant inclusion remains to be mapped. Modulation of fundamental VO_2 properties such as magnitude of switching and $\Delta T_{eq.}$ needs to be investigated for alloyed VO_2 films as a function of substrate coupling.

5.4. Defect Incorporation through Irradiation Exposure

Particulate and electromagnetic irradiation have been used to modulate the structure and MIT characteristics of VO_2. Electromagnetic irradiation generally changes carrier density in

© 2022 Wiley-VCH GmbH

VO_2 and can strongly perturb the electronic structure. X-ray irradiation systematically increases the electrical conductivity of the M1 phase of VO_2 with increasing dose, while modifying the electrical conductivity of the R phase in a somewhat stochastic manner.[168] Upon prolonged X-ray irradiation, $T_{eq.}$ has been found to first increase and then decrease with increasing dose, which has been attributed to the irradiation mediating redox reactions on the vanadium sublattice, which results in self-doping.[169]

Particulate irradiation can be used to increase defect density and modify defect dynamics in VO_2, resulting in substantial alteration of thermodynamic stabilities and transformation pathways. Neutron irradiation has been shown to decrease the electrical conductivity of the M1 phase of VO_2, which is attributed to irradiation-induced creation of defects and expansion of the lattice.[170] In epitaxial VO_2 thin films, proton irradiation systematically increases the electrical conductivity of the M1 phase with increasing ion fluence while decreasing $T_{eq.}$[171] Alpha-particle (He^{2+}) irradiation has been shown to decrease $T_{eq.}$ in freestanding VO_2 nanobeams, while increasing the temperature of the MIT in clamped nanobeams.[39] This phenomenon has been attributed to the creation of vacancy and interstitial defects during irradiation.

Much remains to be explored about how combinations of irradiation exposure and chemical alloying as well as irradiation exposure and strain modify MIT characteristics. Systematic exposure of VO_2 to electromagnetic and particulate irradiation under different boundary conditions holds promise for advancing fundamental understanding of defect formation, defect diffusion, and interactions of point defects with each other and domain boundaries. At the systems level, memristive devices have the potential for greater radiation hardness compared to Si devices and can potentially encode irradiation-induced reconfigurability as an intrinsic functional element.[172]

5.5. Mechanical Resilience of VO_2 Thin Films: Elastic Modulus, Dynamical Evolution of Stress across the MIT, and Fracture Behavior

Given the substantial change in crystal symmetry and lattice volume across the M1–R structural phase transformation and the anisotropic strains engendered in the material, VO_2 films often suffer severe mechanical damage upon thermal cycling.[102,140,141,150,152,173,174] In this section, we review the mechanical properties and deformation behavior of VO_2 thin films.

While mechanical stresses can be used as a tuning parameter for modulating the MIT characteristics of VO_2 (Figure 4),[129,175] thin films are prone to damage if sufficient stresses accumulate during thermal cycling. To accurately determine stress values at a certain level of strain, the elastic modulus of VO_2 must first be determined.[176–179] Singh and Viswanath surveyed the literature and found the elastic modulus of the insulating M_1 phase to range from 100 to 308 GPa based on experiments and first-principles studies.[179] The substantial spread of values derives from differences in geometry, crystal orientation, testing conditions, and fabrication conditions, as well as the potential role of experimental artifacts. In terms of thin films, Rúa et al. reported the elastic modulus of thin films of VO_2-M_1 as 156 ± 7.5 GPa and thin films of Cr-doped VO_2-M_2 as 102 ± 3 GPa based on cantilever resonant frequency measurements.[177] Through nanoindentation at room temperature, Jin et al. reported the "composite" modulus of polycrystalline VO_2 thin films on silicon as 140–170 GPa.[176] With the same technique, the authors also reported the "composite" modulus of epitaxial VO_2 films on sapphire as 240–260 GPa. The "composite" modulus in these studies includes contributions from both the film of interest (VO_2) and the substrate (Si or sapphire). To remove the influence of the substrate and thus measure the intrinsic modulus of VO_2, Zhang et al. utilized the Hay–Crawford thin film model in conjunction with experimental studies, and reported the elastic modulus of VO_2-M_1 and VO_2-R sputtered thin films as 224 ± 20.0 GPa at 25 °C and 210 ± 15.5 GPa at 85 °C.[180] In terms of nanowires, Minor et al. estimated the elastic moduli of VO_2-M_1 and M_2 nanowires to be 128 ± 10 and 156 ± 10 GPa through tensile tests inside a TEM.[13]

It is important to determine stress levels that develop in physically constrained environments during MITs, so as to guide the design of practical neuromorphic devices that avert damage during operation. Zhang et al. utilized a multibeam optical stress sensor to assess the influence of crystal orientation on the stress evolution of VO_2 thin films across repeated structural phase transformations. Textured polycrystalline VO_2 films deposited on Si substrates, as well as epitaxial VO_2 films deposited on sapphire (0001) substrates, develop large tensile stresses when heating through the MIT, whereas epitaxial VO_2 films deposited on TiO_2 (001) substrates develop large compressive stresses in heating through the MIT. This seeming disparity is attributable to the highly anisotropic deformation that occurs during the phase transformation. Mapping atom positions during the phase transformation by reconstructing the transformation tensor corroborates that the strain levels and signs (compression vs tension) are consistent with the experimental observations. These studies highlight the importance of the crystal orientation of VO_2 films on the stress levels developed during thermal cycling, which governs the probability for failure (e.g., fracture primarily as result of tensile stresses). In another study, Viswanath et al. utilized a multibeam optical stress sensor to monitor the stress evolution of polycrystalline VO_2 thin films deposited on Ge(100) substrates during thermal cycling.[181] They found reversible stress evolution over 100 thermal cycles through the MIT in their films.[181] While these results are promising and stress is a useful tunable parameter for modulating phase transformation characteristics, active neuromorphic elements will need to survive many orders of magnitude more on/off cycles. During such long-term cycling, VO_2 films may undergo damage from effects of fatigue. Therefore, studying the fatigue behavior of VO_2 thin films will be critical in designing mechanically robust VO_2 neuromorphic elements.

In terms of fracture behavior, several groups have observed cracking in VO_2 thin films.[102,140,141,152,174,182–184] Nagashima et al. studied epitaxial VO_2 $(40\overline{2})_M$/TiO_2 (001) thin films of various thickness ranging from 10 to 30 nm.[140] Their XRD studies indicated that the crystal structure of the thin films did not change significantly with varying film thickness. However, they found that electrical transport properties changed from a sudden jump in electrical resistivity with temperature to a more complicated multistep process during the MIT with increasing film thickness. Likewise, the on/off ratio of electrical resistivity during the phase transformation decreased with increasing

© 2022 Wiley-VCH GmbH

15214095, 2023, 37, Downloaded from https://onlinelibrary.wiley.com/doi/10.1002/adma.202205294 by Texas A&M University Library, Wiley Online Library on [06/12/2023]. See the Terms and Conditions (https://onlinelibrary.wiley.com/terms-and-conditions) on Wiley Online Library for rules of use; OA articles are governed by the applicable Creative Commons License

film thickness. The authors argued that the disparities between the observed crystal structure (which remained relatively similar with varying film thickness) and transport properties (which changed with varying film thickness) stemmed from the presence of nanoscale cracks, which grew when the film thickness was above 15 nm.[140] Paik et al. reported a similar trend between the on/off ratio of electrical resistivity and critical fracture thickness of epitaxial VO_2 $(40\overline{2})_M$/TiO_2 (001) thin films.[141]

When sufficient lattice strain is induced in VO_2/TiO_2 (001), VO_2 has been found to stabilize as the metallic phase (VO_2-R) at room temperature (and even below).[140] However, under these same conditions, Rodríguez et al. found that VO_2 in regions near a crack existed as the insulating M_1 phase, whereas regions away from the crack existed as the R-phase.[174] This pattern of phase separation can be attributed to the fact that epitaxial lattice strain is relaxed near the cracked region when the film thickness is large enough to induce fracture of the films. As such, it is clear that there is strong interconnectedness and a delicate balance between film geometry (orientation and thickness), fracture, and phase stability (e.g., near/away from fracture regions in which strain is relieved), which correspondingly influence the MIT behavior.

Lattice strain, chemical alloying, and irradiation to induce defects are important tunable parameters for modulating the MIT characteristics of VO_2, and thus neuromorphic function (Figure 4). Lattice strain, while effective in depression/elevation of the $T_{eq.}$, can be relaxed through deformations and is not always equally dispersed throughout the film. Advances in chemical alloying have resulted in identifying the most effective dopants at shifting the MIT but this method introduces large amounts of spatially varying strain on the lattice, which can yield complex stress gradients across phase transformations. Finally, irradiation can not only shift the transition but also increase the conductivity through mediation of redox reactions that introduce charge carriers. However, the effects of irradiation are less predictable and damaging at high energies. In terms of mechanical integrity, we recommend several strategies to move toward damage-free operation of VO_2-based devices. First, decreasing the thickness of the film is an effective technique to reduce the crack driving force and thus avert fracture. Uncracked films have shown better performance characteristics, e.g., on/off ratio. Next, adding an appropriately designed buffer layer between the film and substrate may effectively decrease the lattice mismatch between the VO_2 film and substrate, thereby reducing tensile stresses generated during operation and thus the propensity for fracture. Finally, implementing substrates that possess similar coefficients of thermal expansion to the VO_2 films can minimize thermally induced stresses. Many of these films are fabricated at high temperature; matching the coefficients of thermal expansion of the substrate to the film minimizes thermal stresses that arise during heating/cooling.

6. The Electrically Driven MIT and Electrothermal Couplings in VO_2 Devices

For efficient and fast computational applications, the MIT in VO_2 will need to be driven by an applied electrical bias instead of by indirect thermal activation. Many prior studies have focused on deciphering the origins of the electrically driven transition, which can generally be differentiated into two broad mechanisms: an electronic-structure-modulated MIT versus a Joule-heating-induced MIT. The notion of a carrier-injection-mediated electronic transition is attractive for allowing for delinking of the electronic phase transition from the structural phase transformation, which can enable computing approaches that approach the limits of energy dissipation.[185,186] Proposed mechanisms for this model include carrier injection, photoexcitation, or a percolative-avalanche model.[185–188] However, some of these models have been critiqued for insufficiently considering interfacial thermal resistance or heterogeneous transport. Examples of experimental results include characterization of the electrically driven MIT in which it is found that the electric field needed to induce the phase transition is variable depending on the type of metal used in the electrodes, as well as Raman spectroscopy results showing that the current- or temperature-dependent spectra for the electrically driven MIT do not exactly correspond to the thermally driven MIT.[185,188] With respect to previous electrothermal models of a VO_2 device, localized current density and the formation of R phase channels are not seen.[186,187] An alternative set of mechanisms used to explain the behavior of the electrically driven MIT invokes an electrothermal MIT that is driven by Joule heating.[189–194] Indeed, more recent works attests to Joule heating as the primary mechanism[189–194] in light of linear relationships measured between power dissipated by the device at its critical switching voltage, which is proportional to $V_{crit.}$,[2] and the ambient temperature, from which it is inferred that the temperature at $V_{crit.}$ corresponds to $T_{eq.}$[191,192,195,196] This has further been quantitatively confirmed by direct measurements of the temperature of the material during the electrically driven phase transition, which demonstrates the formation of localized hot filaments.[194,197]

In a two- or three-terminal VO_2 device, the MIT can be triggered by applying either a voltage or current to indirectly heat a volume of VO_2; the two stimuli result in markedly different transformation behavior. The temperature of the device is controlled by the energy balance between the generated heat and the heat dissipated away from the device (see Equation (1)). Under an applied voltage, the phase transformation occurs when the temperature reaches $T_{eq.}$, corresponding to the device's critical voltage ($V_{crit.}$). This coincides with an abrupt increase in the heat generated by the device, which causes a sharp drop of its resistance (**Figure 10**). This causes a feed-forward effect on the temperature of the device, which drives the MIT to some state of completion. When instead a current is applied to the device, the MIT's accompanying drop in resistance decreases or stabilizes the heat generated by the device, allowing the phase change to occur over some range of current values in a feed-back effect (Figure 10).

6.1. Spatial Inhomogeneities in VO_2 under an Electrical Bias

The *I*–*V* response of VO_2 devices is locally active within its region of NDR, meaning that in this region of *I*–*V* space, the VO_2 element itself controls either the net current through

© 2022 Wiley-VCH GmbH
15214095, 2023, 37, Downloaded from https://onlinelibrary.wiley.com/doi/10.1002/adma.202205294 by Texas A&M University Library, Wiley Online Library on [06/12/2023]. See the Terms and Conditions (https://onlinelibrary.wiley.com/terms-and-conditions) on Wiley Online Library for rules of use; OA articles are governed by the applicable Creative Commons License

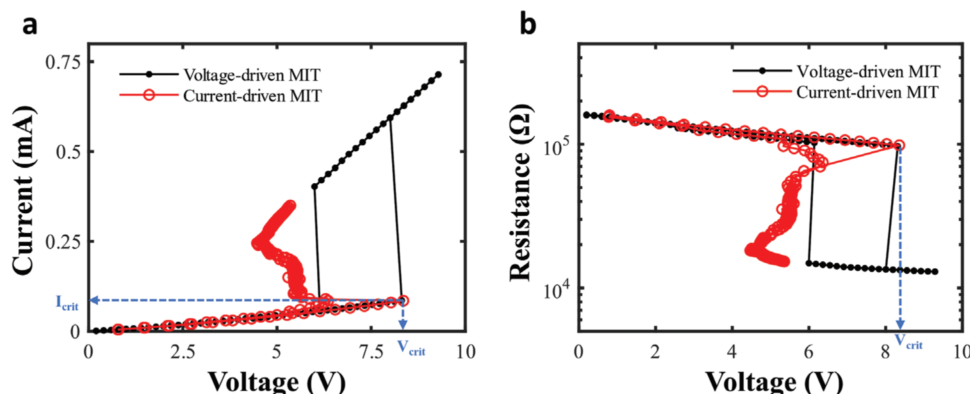

Figure 10. Voltage- and current-driven MIT in VO_2. a) Current–voltage response of voltage- (black) and current-driven (red) MITs in a VO_2 thin film device fabricated from a 100 nm polycrystalline VO_2 thin film deposited using reactive magnetron sputtering. The critical switching voltage ($V_{crit.}$) and critical switching current ($I_{crit.}$) are labeled. While the voltage-driven MIT occurs abruptly, the current-driven MIT occurs over a range of current values. b) This phenomenon is seen also in the measured resistance of the device through the phase change, as the resistance value of the device changes abruptly in the voltage-driven MIT but gradually over a range of values in the current-driven MIT.

the circuit (when the external source is an applied voltage) or the voltage across each circuit component (when the external source is an applied current).[8] NDR refers to an electrical resistance which decreases as a function of an increasing applied electrical bias

$$\frac{dI}{dV} < 0 \tag{8}$$

NDR can be found in materials that form higher current density channels relative to the rest of the material under the application of an electrical bias.[50] The formation of conductive channels of R phase VO_2 has been demonstrated through different methods (**Figure 11**).[190,195,197–199] These filaments can be observed optically as a result of the difference in reflectivity between the two phases. Spatial mapping of X-ray signals also reveals localized formation of the R phase.[200] Phase coexistence during the electrically driven transition has interesting implications with respect to tailoring the device behavior toward specific desired properties. For instance, with control over the total volume of VO_2 undergoing the MIT, the conductance differentials between heterogeneous phase domains become tunable with domain periodicity, affording finer control over the delay time for switching the device.

Altering the size of the conductive channel is crucial to the performance of the device. It has been demonstrated that after the appearance of the conductive channel, additional application of electrical stimuli tends to widen the channel.[197,201] Other studies have focused on tuning the size of the conductive channel using different series resistors, thereby modulating the ratio of M1 to R phase present in the device based on the ability to control the dimensions of the ON-state channel.[192,200] The size of the channel is also dependent on the device geometry, as there is a linear relationship between device length and channel

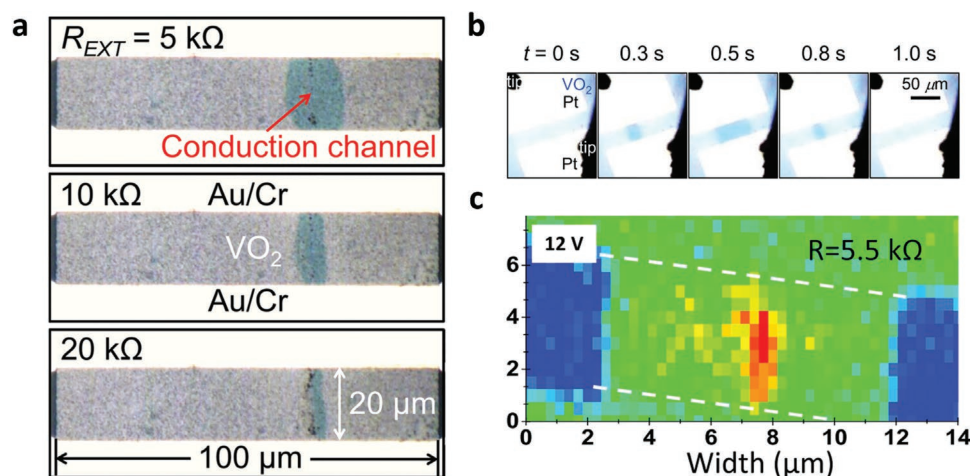

Figure 11. Inhomogeneity in the MIT. Several methods have been used to characterize the emergence of spatial inhomogeneities across the electrically driven MIT. a) Optical images show that the width of a conduction channel can be tuned by the magnitude of the external load resistor. Reproduced with permission.[196] Copyright 2014, AIP Publishing. b) Other optical studies focus on the delay time of the onset of the filament formation. Reproduced with permission.[190] Copyright 2013, AIP Publishing. c) The phase of the conductive filament has been confirmed to be rutile VO_2 by spatial mapping of X-ray analysis. Reproduced with permission.[200] Copyright 2013, AIP Publishing.

15214095, 2023, 37, Downloaded from https://onlinelibrary.wiley.com/doi/10.1002/adma.202205294 by Texas A&M University Library, Wiley Online Library on [06/12/2023]. See the Terms and Conditions (https://onlinelibrary.wiley.com/terms-and-conditions) on Wiley Online Library for rules of use; OA articles are governed by the applicable Creative Commons License

15214095, 2023, 37, Downloaded from https://onlinelibrary.wiley.com/doi/10.1002/adma.202205294 by Texas A&M University Library, Wiley Online Library on [06/12/2023]. See the Terms and Conditions (https://onlinelibrary.wiley.com/terms-and-conditions) on Wiley Online Library for rules of use; OA articles are governed by the applicable Creative Commons License

width, but relatively little correlation between device width and channel width.[196,202] Another study shows that whereas for larger devices ($L > 10$ µm), the channel appears at the same position each cycle, for smaller devices ($L \leq 10$ µm), there is some stochasticity in the position of the channel from one cycle to another.[196]

6.2. Energy Efficiency and Switching Speed of VO_2 Devices

Improved control of VO_2 MIT transformation characteristics is critical to the design of neuromorphic device elements that overcome the prohibitive bottlenecks faced by digital AI at all levels of the stack. To realize the full promise of neuromorphic computing, new algorithms and computing architectures will also need to be codesigned alongside circuits that exploit the tunable characteristics of the VO_2 MIT. A deeper discussion of the fundamental approaches behind historical and current artificial neural network models and modularized neuronal and synaptic hardware development has recently appeared elsewhere.[34] To compute the energy advantages of individual stack components, a rigorous evaluation of switching energy and speed is required, albeit such projections are most useful when a functional chip-scale computing advantage can be evaluated. **Table 1** presents a compendium of switching energies and times found and inferred from the literature for VO_2 devices as a function of device dimensions. In general, the switching energy and speed of VO_2 compares favorably with that of the Peierls' insulator NbO_2, whose much higher MIT temperature requires 6× the energy and 100× the switching time.[8] In order to develop accurate stack-level projections, the energy and time scaling of electrical switching in VO_2 must be better understood in terms of the various parameters that affect these outputs. These parameters include external circuit elements, ambient temperature of the device, device geometry, and device thermal and electrical properties as well as the MIT and material properties of VO_2 (which are tunable based on the parameters shown in Figure 4).

6.3. Electrically Driven MIT in Undoped VO_2 Particles and Thin Films

Different aspects of the electrically driven MIT can be tuned to modulate VO_2 device performance. The morphology of the active element is a major determining factor in its response to electrical stimuli. Nanobeam prototype devices are of interest in fundamental materials research as they behave like quasi-1D structures that are confined along two out of three dimensions and can be strained along specific axes.[125,195,207] For thermal triggering of phase transitions, this is manifested in abrupt, single-step MIT behavior for undoped and unstrained VO_2 single crystal nanostructures, which are further characterized by a large R_{ON}/R_{OFF} ratio between the two resistance states.[104,125] When the transition is electrically induced in unstrained single-crystal VO_2 particles, a striped pattern of M1 and R phases emerges instead of the channel formation observed in thin film devices, and reflects the balance between interfacial coherency strains and beam deformation.[195,208] This results in a stepwise sequence of resistance states, which stands in contrast with the single-step phase transition behavior observed in the thermally driven MIT.[60]

In VO_2 thin films, a comparison can be made between the properties of polycrystalline thin films and epitaxial or single-crystal thin films because properties such as grain size, defect density, and crystal orientation of the films affect their thermally driven MIT properties such as the R_{OFF}/R_{ON} ratio, $T_{eq.}$, and hysteresis.[123,193,194] However, it is challenging to make a direct comparison between polycrystalline and epitaxial thin film device responses to electrical stimuli, since it can be difficult to disentangle the role of film texture from extrinsic parameters such as device dimensions. While $V_{crit.}$, $I_{crit.}$, and $T_{eq.}$ can be compared directly, it is unclear how other characteristics, such as hysteresis, directional electrical conductivity, and single-phase electrical conductivities will affect the electrically driven MIT, in addition to the effects caused by differences in thermal properties between a deposited VO_2 layer and its substrate. Additionally, the role of crystallinity and texture of VO_2 on formation of conductive channels remains unexplored.

6.4. Effect of Site-Selective Modification on VO_2 Device Behavior

The incorporation of dopants can alter VO_2 device response to electrical stimuli. Tungsten-doped VO_2 nanobeams and nanofilms exhibit decreasing $V_{crit.}$ as a function of increasing W concentration, which is correlated to a lower $T_{eq.}$ as compared to undoped VO_2.[209,210] In contrast to the linear relationship between $V^2_{crit.}$ and temperature in undoped VO_2, the critical switching voltage for the MIT in W-doped VO_2 follows an

Table 1. Examples of energies and times to switch VO_2 devices. L, W, and t refer to length, width, and thickness, respectively, where L is the distance between the two electrodes. Additional factors that would affect the switching energy and time, but are not listed in this table, include the ambient temperature of the device, device properties such as interfacial thermal resistances, and the variable interfacial and material properties of the VO_2 films used to make these devices. Where the energy of the device was not found in the text, the power to switch the device was multiplied by the switching time to provide a value for the switching energy.

Device geometry	L	W	t	Switching time	Switching energy	Refs.
Planar	3 µm	30 µm		9 ns	0.35 nJ	[203]
Planar	0.2 µm	2 µm	50 nm	100 ns	8.58 nJ	[193]
Through-plane	d = 0.2–1 µm	d = 0.2–1 µm	400 nm	1.9 ns	0.11 nJ	[204]
Nanogap	125 nm			5 ns		[205]
Nanochannel	d = 10 µm	d = 10 µm	80 nm	17 ns	8 pJ	[206]

 © 2022 Wiley-VCH GmbH

exponential dependence on ambient temperature, whereas the MIT manifests a square-root

$$V_{\text{crit.}} \propto \sqrt{T_{\text{MIT}} - T_{\text{amb.}}} \tag{9}$$

relationship with ambient temperature.[209] By contrast, chromium-doped VO_2 thin films exhibit a lower $V_{\text{crit.}}$ as compared to undoped VO_2 despite having a higher $T_{\text{eq.}}$.[211] Inclusion of the interstitial dopant boron in VO_2 protodevices has been shown to create a time-dependent relaxation effect that is measurable in the electrically driven MIT.[74,87] Inclusion of boron also creates pinning sites that cause the phase transition to occur in a step-like manner over a range of applied current or voltage values.[212] While information on the thermally driven MIT for doped VO_2 is extensive, the electrically driven MIT of doped VO_2 thin films remain relatively underexplored.

6.5. Nonvolatile Memory Storage and In-Material Processing in VO_2

Nonvolatile memory in neuromorphic computing is inextricably tied to state hysteresis, and, consequently, control over transition hysteresis properties is important to neuromorphic material design. The transition hysteresis is integral to the neuromorphic computing capability of VO_2 because it enables on/off (R-phase/M1-phase) state retention in the absence of exciting stimuli. A narrow hysteresis requires little energetic overpotential to initiate transitions between on/off states, and, consequently, the states may be easily and efficiently overwritten. By contrast, a wider hysteresis requires greater energetic overpotential to initiate transitions, and, consequently, the material state is retained with greater resilience against low-energy stimulus fluctuations. VO_2 is a promising candidate for integration within a broad range of neuromorphic architectures owing to its near-room-temperature MIT, but is also constrained with regards to the hysteresis width as compared to other candidates such as NbO_2 characterized by a Mott transition or HfO_2 where memristive behavior is underpinned by oxygen vacancy formation and diffusion. The challenges in imbuing nonvolatile memory storage are a limitation to the integration of VO_2 in numerous device architectures.

All-thermal, nonvolatile multilevel memory has been demonstrated as enabled by hysteretic radiative heat transfer between deposited VO_2 and its fused quartz substrate.[213] All-electrical, nonvolatile memory in VO_2 has been enabled in practice by sustaining a low voltage bias, which in turn induces self-Joule heating that raises the temperature to a value sufficiently centered within the VO_2 hysteresis.[214] At this voltage bias and consequent operating temperature, any M1 and R phase VO_2 present is sustained. Further over- and underpotentials (≈±0.3 V) are needed to switch between low- (R) and high- (M1) resistance states, respectively.[214] Transitions between these two states can be controlled by voltage pulses (to induce the R phase) or by zero-bias-voltage pulses (to return to the M1 phase). Partial transformation within a single particle is possible by applying low-energy pulses deviating from the operating voltage bias, which can provide access to a range of functional resistance values.[214]

As illustrated in Figure 1B, nonvolatile states have been defined by coupling to a dynamical chemical change such as inducing oxygen vacancies through ionic-liquid gating with state retention spanning multiple days albeit the write/read dynamics are slow, on the order of tens of minutes.[64,215,216] Erasure is achieved through thermal annealing. Dynamical dopant incorporation has been used to imbue nonvolatility by annealing under H_2.[162] The process takes on the order of hours and is reversible upon thermal annealing. Coupling to remnant strain fields on ferroelectric substrates further imbues some degree of nonvolatility with write/erase times on the order of minutes.[217] As will be described in a subsequent section, Jung et al. have demonstrated a sub-150 µs optical write/erase approach that is based on accessing a metastable excited state; dynamical oscillations constitute the readout and can be retained for over 3 days; erasure is achieved by a current pulse.[215] The substantial control over hysteresis widths accessed through site-selective modification discussed in preceding sections affords opportunities for systematically tuning nonvolatility through codoping with oxygen vacancies, interstitial hydrogen or boron, or Li-ions.

As sketched in Figure 1B, in-material processing through dynamically reversible chemical changes induced through ionic-liquid-mediated oxygen vacancy formation,[64,216] incorporation of interstitial hydrogen,[162] proton- or Li-ion insertion,[65] or photochemically induced structural transformations[215] provides a means of engendering synaptic functionality with variable plasticity profiles. Control of nonvolatile memory through in-material processing serves as a means of coupling to optical and strain fields or electrochemical modulation of volatility and is a key part of the arsenal for tuning transformation characteristics to realize the full promise of VO_2 in neuromorphic architectures.[218] Indeed, by utilizing ionic gel and electrochemical proton doping, multineuron VO_2 transistors have achieve several synaptic functions such as pair-pulse facilitation, long-term potentiation, long-term depression, spike-rate-dependent plasticity, and spike-timing-dependent plasticity.[219] Another synaptic transistor utilized a combination of proton intercalation and oxygen vacancies to accelerate proton insertion.[66]

6.6. VO_2-Based Devices with Unconventional Device Configurations

Distinctive device geometries and form factors can be used to leverage VO_2 transformation characteristics to achieve unusual functionality. Several strategies have been demonstrated to reduce $V_{\text{crit.}}$ for VO_2 devices. In particular, compressive strain can be used to suppress $V_{\text{crit.}}$. A significant decrease of $V_{\text{crit.}}$ is observed for VO_2 nanobeams under compressive strain.[124] Similarly, microtube devices formed out of VO_2 nanomembranes have a compressive, external strain that monotonically decreases the onset voltage necessary for the film to switch.[220] Composite VO_2–carbon nanotube devices, which utilize a carbon nanotube as a heater parallel to the direction of current flow, require less energy input to initiate the phase transition.[48] Dual-mode VO_2/HfO_2 neurons have been constructed and feature finely tunable VO_2 firing thresholds (1.8–2.4 V) based on altering the conductance of the HfO_2 dielectric layer.[221] These

© 2022 Wiley-VCH GmbH

15214095, 2023, 37, Downloaded from https://onlinelibrary.wiley.com/doi/10.1002/adma.202205294 by Texas A&M University Library, Wiley Online Library on [06/12/2023]. See the Terms and Conditions (https://onlinelibrary.wiley.com/terms-and-conditions) on Wiley Online Library for rules of use; OA articles are governed by the applicable Creative Commons License

examples illustrate the potential of heterostructures with appropriately matched interfaces to selectively tune VO_2 transformation characteristics.

Conversely, several strategies have been put forth to push the $V_{crit.}$ to higher values. The selective oxidation of a domain has been used to elevate the transition temperature.[222] $V_{crit.}$ increases upon use of a dielectric layer between the electrical source and the VO_2 thin film.[223] While these configurations may be less applicable for on-chip integration, they provide valuable information on further ways to tune VO_2 device properties.

Many intrinsic material properties play into the behavior of a VO_2 device, such as the electrical and thermal conductivities of VO_2 and its distinctive set of MIT characteristics such as $T_{eq.}$, hysteresis, conductance contrast, and sharpness of onset (Figure 1). However, extrinsic device properties such as the geometry of the device and the matrix in which the active VO_2 volume is embedded play an equally important role in governing the response of the device to electrical stimuli (Figure 4). Finally, circuit components such as load resistors, extrinsic or intrinsic capacitance of the system, type of applied electrical bias and its time-dependence (applied voltage vs applied current; steady-state, quasi-steady, or dynamical electrical measurements) also alter the device response (**Figure 12**). The number and complexity of these interconnected parameters make prediction of the electrical response of a VO_2 device difficult. For example, some relationships between parameters are well characterized, such as the relationship between temperature and electrical conductivity for various morphologies of VO_2 and doped VO_2 systems. However, in a device this relationship is further complicated by a feedback effect between temperature, electrical conductivity of the material, power dissipated within the device, and finally heat conducted away from the active volume of the device. The time-variant modulation of these properties and their coupling can give rise to dynamical responses such as oscillations discussed in preceding sections. While certain device relationships have been characterized, such as the relationship between $T_{eq.}$ and $V_{crit.}$ of a device, other relationships are less intuitive to disentangle, such as the relationship between the load resistance of the circuit and the formation of spatial inhomogeneities. To further investigate the full capabilities of VO_2 devices, the interconnected relationships between intrinsic and extrinsic device and circuit parameters must be mechanistically understood and deterministically controlled.

To be technologically relevant, VO_2 thin film devices must be developed with increasingly small device dimensions. They must require as little energy input as possible to achieve their

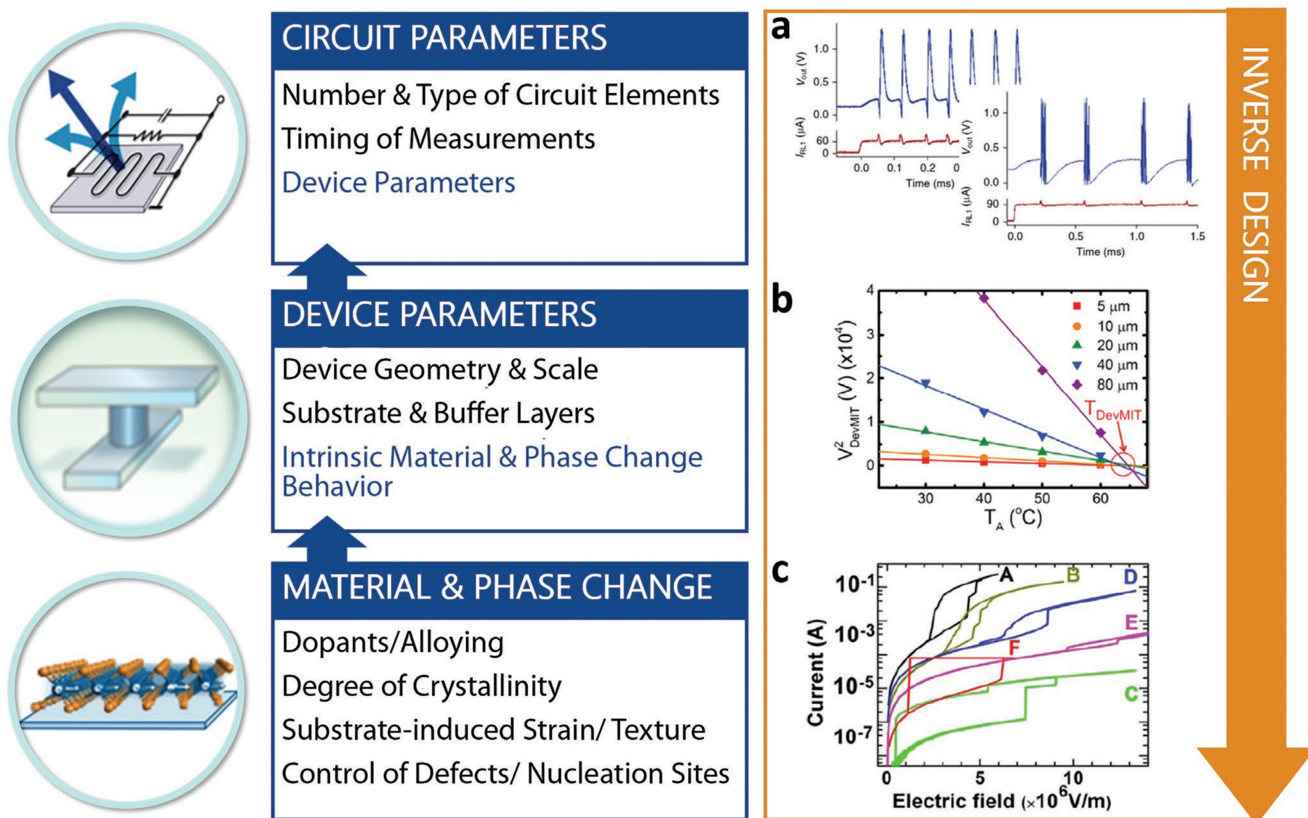

Figure 12. Hierarchical interactions between intrinsic material properties and phase change behavior, device parameters, and circuit level parameters. Critical design variables exist at each level of the hierarchy, which impact the ultimate electrical response of the system. a) Tonic spiking and tonic bursting behavior resulting from different circuit capacitance and resistance. Reproduced with permission.[8] Copyright 2018, Springer Nature. b) Critical transformation voltage as a function of device size and ambient temperature. Reproduced with permission.[196] Copyright 2014, AIP Publishing. c) Intrinsic current–voltage response of VO_2 thin films, as a result of deposition parameters, which impact film microstructure, defect concentrations and other structural film aspects. Reproduced with permission.[204] Copyright 2013, IEEE.

© 2022 Wiley-VCH GmbH

15214095, 2023, 37, Downloaded from https://onlinelibrary.wiley.com/doi/10.1002/adma.202205294 by Texas A&M University Library, Wiley Online Library on [06/12/2023]. See the Terms and Conditions (https://onlinelibrary.wiley.com/terms-and-conditions) on Wiley Online Library for rules of use; OA articles are governed by the applicable Creative Commons License

desired device performance. They will have high operating temperatures and fast response times. Key areas of future development include quantifying the relationships between device properties and parameters and desired electrical performance, as well as devising a method for increasing the operational temperature of the device. Further investigation into the time-dependence of material properties and device behaviors characteristics, such as switching times, time-dependent heat transfer from a device, and frequency of device switching, is essential. As both intrinsic and extrinsic properties are at play, an exhaustive characterization of these relationships requires both experimental and computational approaches bridging across decades of length and time scales.

7. Optically Driven MIT, Associated Structural Rearrangements in VO_2, and Implications for Neuromorphic Perception Systems

The burgeoning role of photonic memristors in neuromorphic computing architectures is an exciting prospect recently reviewed by Goi et al.[224] The optically triggered MIT of specifically VO_2 is notable for its rapid (as fast as ≈26 fs), single-photon Mott–Hubbard transition from an insulating state to a metallic state.[225] Ultrafast electron diffraction coupled to time-resolved infrared transmittance measurements reveals the emergence of a metallic state with a distinctive dielectric signature (optical bandgap below 0.25 eV) while a metastable M1 structure of VO_2 persists.[226] Radial pair distribution difference function measurements indicate valence charge density increases in the V–V dimerized bond (derived from d_{xy} subshell interactions) upon photoexcitation, concomitant with d_{xz} subshell (associated with octahedrally chained V and O atoms) charge density reduction.[226] This indicates an electronic transition in VO_2 occurs during the optical MIT prior to the full structural rearrangement from M1 to R phase and furthermore suggests that the latent heat of the thermally activated MIT is largely necessary for the structural transition rather than electronic transition.[226]

Photoexcitation fluence provides a convenient control over induction of either solely electronic versus a coupled electronic and structural transition.[226,227] Morrison et al. found that at 800 nm wavelength excitation, a pump fluence >9 mJ cm^{-2} was sufficient to trigger structural reordering; electronic transitions to a more metallized configuration were accessible at pump fluences as low as 2 mJ cm^{-2}.[226] At the higher fluence, disrupting the atomic ordering to yield R phase occurred over ≈300 ps.[226] Once formed, the metallic VO_2 state is stabilized by ligand-to-metal charge-transfer-type transitions (O 2p to V 3d bands), allowing the state to persist on a comparatively long-lived picosecond timescale before relaxing back to the insulating electronic state (and M1 phase).[225] The longevity of the optically transitioned state is posited to electron–phonon carrier relaxation pathways.[226] The pump fluence furthermore influences domain heterogeneity during the photoinduced transition, yielding insulating and metallic domains spatially separated on scales of ≈100 nm.[225,228] Similar fluence-dependent inhomogeneity was observed even within individual single crystals of VO_2, suggesting fluence is a leading tunable parameter for dynamically modulating localized electronic transitions upon optical excitation.[227] Optical excitation affords a means of addressing a primary drawback of VO_2 as a memristor or oscillator network, difficulties in imbuing nonvolatile memory. Recent work has demonstrated that optical excitation can be used to stabilize a putative metastable excited state that persists at room temperature and under ambient conditions even without continued photoexcitation or electrical bias. The optical memory is addressed and read at <150 µs times in the form of voltage oscillations between the insulating and metallic states.[215]

All-optical infrared-switching VO_2 devices in relatively simple configurations feature coupling to Si waveguides.[229,230] Under voltage bias, VO_2/Si devices can operate under low energy requirements (as low as 23.5 pJ per pulse) for writing memory with good retention (over 200 h) of the memory state.[230] Reproducibility for such devices has been shown over 10 000 write/erase instances.[230] Further VO_2 optical device adaptations have been designed using metasurfaces to control optical coupling through the use of bespoke plasmonic meta-atoms.[231,232] Au was shown an advantageous metaelement to align surface plasmon resonance wavelengths to photoexcitation sources in a study utilizing a perforated top film that achieved 50% power reduction to induce the VO_2 MIT.[231] A related device advanced by integration to a Ti/Au/VO_2/Ti/Au threshold switching selector enabled promising control of MIT transition characteristics and ultimately produced an optical system capable of image processing tasks.[232] Material pairings with VO_2 to form p–n heterojunctions have been realized in WSe_2/VO_2 heterostructure devices capable of switching between photovoltaic and photoconductive detection modes upon transformation from insulating to metallic phases, respectively.[233]

A mixed optical/CMOS-integrated device has been designed based on three VO_2 oscillators to construct an optical recognition system.[234] The circuit stores training data as coupling weights of the VO_2 oscillators. The image sought to be examined is encoded in the form of time delays in oscillator inputs; phase differentials in oscillator waveforms are used to reconstruct the image. A particularly compelling demonstration of the utility of optically coupled VO_2 devices comes from the work of Yang and co-workers who recently demonstrated a spike-based neuromorphic perception module based on high-quality epitaxial VO_2 thin films with high conductance contrast and sharp onset temperatures. By coupling the nonlinear VO_2 device element with calibration and scaling resistors and an arrays of sensors, the researchers were able to encode illuminance, temperature, pressure, and curvature signals in the spiking response, enabling identification of hand gestures as required for haptics applications with the use of spiking neural networks.[235]

8. Conclusions and Outlook

A four-to-five orders of magnitude improvement in energy consumed and time-to-solution for the same problem has been projected for neuromorphic computing over current digital computing based on the design of new circuit elements that

© 2022 Wiley-VCH GmbH

15214095, 2023, 37, Downloaded from https://onlinelibrary.wiley.com/doi/10.1002/adma.202205294 by Texas A&M University Library, Wiley Online Library on [06/12/2023]. See the Terms and Conditions (https://onlinelibrary.wiley.com/terms-and-conditions) on Wiley Online Library for rules of use; OA articles are governed by the applicable Creative Commons License

leverage Mott transitions, embedding a nontrivial number of such circuit elements in CMOS-integrated networks, and operating them using algorithms purpose-designed for nondigital devices.[15,236,237] The predicted improvements result from computations being performed in an entirely different way from a digital platform at all levels of the stack. Beyond energy efficiency, considerable excitement about the promise of neuromorphic computing arises from prospects of realizing altogether new function. Brain-inspired computing holds promise for integrating sensing capabilities with logic and memory, thereby enabling 3D spatiotemporal perception in a manner available to biological organisms. This could take the form of relatively simple edge computing to determine the most valuable information for further retention and processing or implementation in autonomous vehicles, robotic systems, or the idea of “complementary intelligence” bridging human and machine intelligence.[238]

Realizing the full promise of neuromorphic computing requires deciphering and precisely modulating the mechanisms of electronic instabilities that are at the heart of low-entropy electronic transitions such as the Mott–Peierls transition of VO_2. Approaching the fundamental limits of energy efficiency and speed possible using VO_2 as an active neuromorphic element necessitates control over the specific compositional, structural, and mesoscale levers for tuning phase stabilities, transformation pathways, and nucleation mechanisms illustrated in Figure 4. In this article, we have reviewed current understanding of the role of nonlinear dynamical transitions in neuromorphic computing, tracing the connections between neuronal and synaptic function and intrinsic material properties and their coupling through interfaces with photoexcitation and voltage, temperature, and strain fields (Figure 2). We have further examined current ideas of transformation mechanisms in VO_2 and opportunities for modifying the transformation characteristics of this material by site-selective modification (substitutional or interstitial doping), defects, and strain (external, chemical, or epitaxial). A curated set of examples from the literature have been used to describe processing–structure–property relationships for single-crystalline nanostructures and VO_2 films with a specific emphasis on the role of boundary conditions. In addition to the modification of MIT characteristics by substrate coupling, we have highlighted the dynamical evolution of stress across the MIT in the context of device resilience.

Figure 13 illustrates open questions and research opportunities related to understanding and modulating the MIT of VO_2 across decades of length and time scales through control of material properties, as well as modes and strengths of coupling to external composition, strain, thermal, and electric fields (Figure 2). A key gap, outlined in Section 2, pertains to the limited current knowledge of how to map specific neuromorphic function to intrinsic material, compositional, and interface properties. As noted above, channel formation means transport in devices is nonuniform, and first-order transitions are accompanied by some extent of hysteresis. A critical need is to derive atomistic understanding of the dynamical evolution of atomic connectivity and electronic structure in active channels using methods such as operando scanning transmission electron microscopy and X-ray ptychography in conjunction with electrothermal measurements. Standardization of such measurements across the field is imperative to benchmark accessible limits of energy efficiency and speed-up.

From the perspective of inverse design, several questions remain, for instance, 1) a priori prediction of the temporal characteristics of VO_2 circuit elements, e.g., periodic versus bursting versus chaotic,[239] or 2) additional dynamical degrees of freedom that can be enabled within a network integrating a nontrivial ensemble of circuit elements as opposed to an individual device. A growing body of experimental work shows that these factors are closely interrelated.[236] An attractive approach to address the complexity of inverse design of neuromorphic device elements across scales is to leverage carefully constructed libraries with site-selective modification and systematic variation of circuit parameters, and with the help of Bayesian machine learning (ML) and multimodal operando measurements, connect target neuronal behavior to the necessary material properties. To navigate the vast available design space, it will be important to design algorithms to express the physical/chemical features of materials that best underpin a specific neuronal function. Such an approach can address challenges with inverse design resulting from the large dimensionality of the feature space, the sparsity of available data, and the fact that the region of interest with desirable properties is often a narrow singularity. For instance, such an approach can inform the design of codoping schemes (Equations (4)–(6)) or guide the use of a specific directional strain field to couple with a specific doped VO_2 film under certain geometric constraints (Figure 7).

Strain plays a key role in altering the electronic properties of VO_2. First, strain couples directly to electronic transformations by modifying VO_2's lattice and electronic structure. Strain is also ever-present in realistic device structures, e.g., in residual strains induced during fabrication, such as those stemming from epitaxy. As such, electronic properties of VO_2 can potentially be tailored by displacing atoms through controlled mechanical strain, either external strain applied dynamically, e.g., via a piezoelectric actuator, or built-in statically, e.g., via epitaxy. Particularly tantalizing, these strains may directly induce a phase transformation (e.g., by piezoelectric actuation) or may poise VO_2 at the cusp of a phase transformation or electrical instability, thereby dramatically reducing the energy and time required to switch states. However, fully harnessing these effects in a deterministic manner requires a deeper mechanistic understanding of the mechanoelectronic interplay in VO_2 and is thus a key topic of future studies. For instance, does strain induced by doping of VO_2 directly influence electronic switching (e.g., from the strain level itself) or are these effects more indirect, e.g., by the dopant serving as a nucleation site for the transformation?

Another emerging frontier relates to the design of complex ternary or quaternary vanadium oxides with precisely tunable charge- and spin-ordering motifs that afford a still broader range of phase transformation mechanisms (Figure 13, right). In $M_xV_2O_5$ and $M_xM'_yV_2O_5$, where M and M′ represent s-, p-, or d-block ions, x and y are their respective stoichiometries, and V_2O_5 represents one of several possible polymorphs, the manifestation of mechanisms such as polaron oscillation, lone-pair anharmonicity, and canonical Mott transitions provide a basis for conductance switching across a broad range of critical temperature, current, and voltage values.[7,240,241] In these compounds, Li-ion or proton intercalation can bring about

© 2022 Wiley-VCH GmbH

15214095, 2023, 37, Downloaded from https://onlinelibrary.wiley.com/doi/10.1002/adma.202205294 by Texas A&M University Library, Wiley Online Library on [06/12/2023]. See the Terms and Conditions (https://onlinelibrary.wiley.com/terms-and-conditions) on Wiley Online Library for rules of use; OA articles are governed by the applicable Creative Commons License

15214095, 2023, 37, Downloaded from https://onlinelibrary.wiley.com/doi/10.1002/adma.202205294 by Texas A&M University Library, Wiley Online Library on [06/12/2023]. See the Terms and Conditions (https://onlinelibrary.wiley.com/terms-and-conditions) on Wiley Online Library for rules of use; OA articles are governed by the applicable Creative Commons License

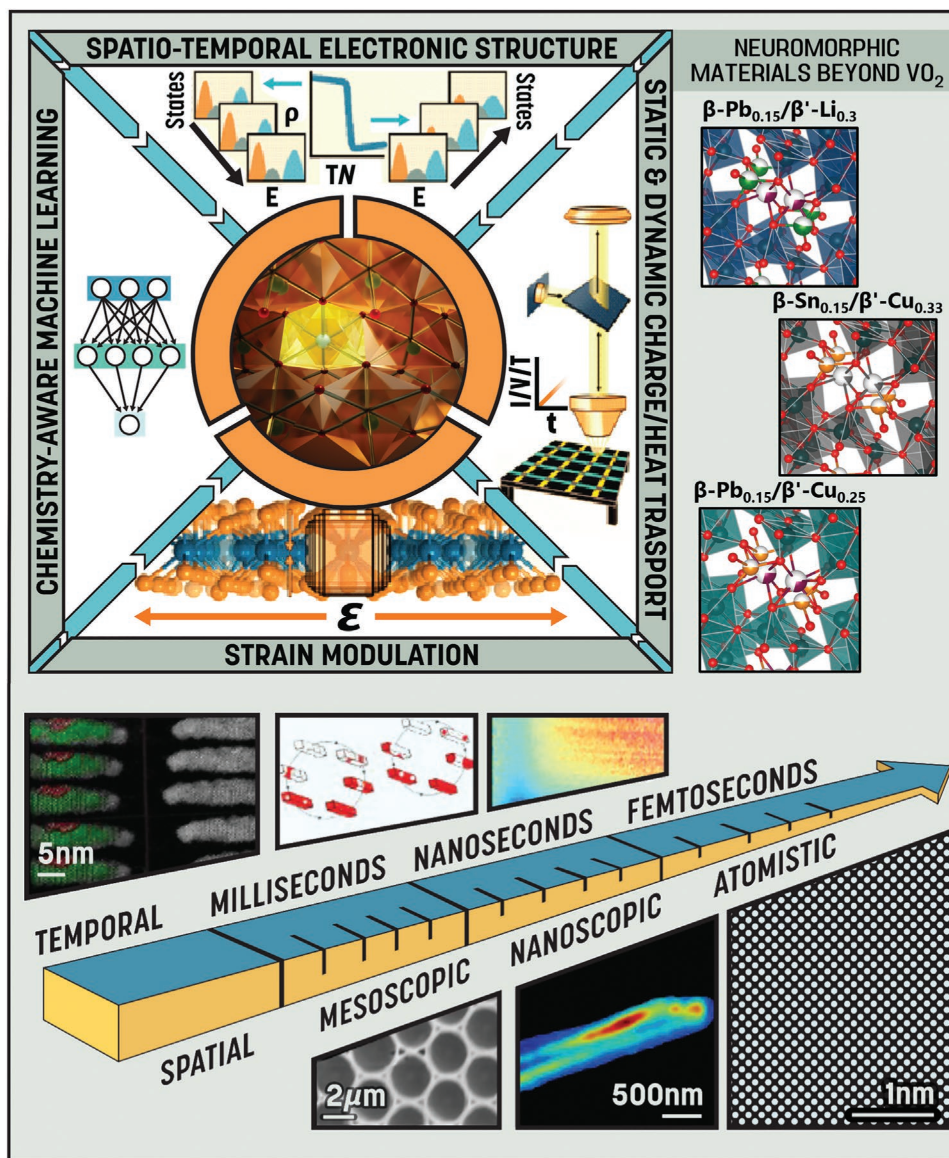

Figure 13. Challenges and opportunities for designing neuromorphic elements from VO_2. The microscopic response of VO_2 to an external stimulus (electric field, temperature gradient, elastic strain, etc.) results from a complex interaction between intrinsic material properties, properties of surrounding materials (e.g., contacts and substrate) and interfaces, and the external stimulus itself. Predicting the response of a material system (and designing a material to exhibit a particular response) across multiple decades of length and timescales requires multiscale, multiphysics models informed by operando measurements of spatiotemporally resolved electronic structure and electrothermal transport. External stimuli operate on a material to change its internal structure, which in turn alters the microscopic properties of a particular volume of material. These changes in structure occur across multiple length-scales. Chemistry-aware machine learning techniques can be used in conjunction with analytical frameworks and operando measurements to accurately predict a material response to a particular set of external fields. Lower-half, top, left panel reproduced with permission.[71] Copyright 2017, Springer Nature; lower-half, top, middle panel reproduced with permission.[40] Copyright 2018, American Chemical Society; lower-half, bottom, left and middle panels reproduced with permission.[243] Copyright 2020, Elsevier.

reconfigurability across different regions of the phase diagram, enabling toggling between neuronal (thresholding, amplification, integration) and synaptic (learning, memory) modes.[242]

Supporting Information

Supporting Information is available from the Wiley Online Library or from the author.

Acknowledgements

This research was primarily supported by Texas A&M X-Grants. S.B, P.J.S., P.S., A.B., and R.M.G. acknowledge the Data-Enabled Design and Discovery of Energy Materials fellowship funded under National Science Foundation (Award No. DGE-1545403). This material is based upon work supported by the National Science Foundation under Grant No. DMR-1847956 (P.J.S.). S.B. further acknowledges support from the Welch Foundation. The authors thank David Santos and Joseph V. Handy for assistance in figure preparation.

15214095, 2023, 37, Downloaded from https://onlinelibrary.wiley.com/doi/10.1002/adma.202205294 by Texas A&M University Library, Wiley Online Library on [06/12/2023]. See the Terms and Conditions (https://onlinelibrary.wiley.com/terms-and-conditions) on Wiley Online Library for rules of use; OA articles are governed by the applicable Creative Commons License

Conflict of Interest

The authors declare no conflict of interest.

Keywords

doping, electronic structures, metal–insulator transition, Mott transition, neuromorphic computing, phase transition, vanadium dioxide

Received: June 12, 2022
Revised: August 2, 2022
Published online: November 29, 2022

[1] R. Vinuesa, H. Azizpour, I. Leite, M. Balaam, V. Dignum, S. Domisch, A. Felländer, S. D. Langhans, M. Tegmark, F. F. Nerini, *Nat. Commun.* **2020**, *11*, 233.
[2] N. C. Thompson, K. Greenewald, K. Lee, G. F. Manso, *IEEE Spectrum*September **2021**.
[3] R. Roscher, B. Bohn, M. F. Duarte, J. Garcke, *IEEE Access* **2020**, *8*, 42200.
[4] Cisco, *Global Cloud Index: Forecast and Methodology*, **2018**.
[5] E. Masanet, A. Shehabi, N. Lei, S. Smith, J. Koomey, *Science* **2020**, *367*, 984.
[6] I. K. Schuller, R. Stevens, R. Pino, M. Pechan *Neuromorphic Computing: From Materials to Systems Architecture Roundtable*, USDOE Office of Science, Gaithersburg, MD **2015**.
[7] J. L. Andrews, D. A. Santos, M. Meyyappan, R. S. Williams, S. Banerjee, *Trends Chem.* **2019**, *1*, 711.
[8] W. Yi, K. K. Tsang, S. K. Lam, X. Bai, J. A. Crowell, E. A. Flores, *Nat. Commun.* **2018**, *9*, 4661.
[9] J. Torrejon, M. Riou, F. A. Araujo, S. Tsunegi, G. Khalsa, D. Querlioz, P. Bortolotti, V. Cros, K. Yakushiji, A. Fukushima, H. Kubota, S. Yuasa, M. D. Stiles, J. Grollier, *Nature* **2017**, *547*, 428.
[10] M. Lundstrom, *Science* **2003**, *299*, 210.
[11] G. M. Moore, *Electronics* **1965**, *38*, 114.
[12] R. H. Dennard, F. H. Gaensslen, H.-N. Yu, V. L. Rideout, E. Bassous, A. R. LeBlanc, *IEEE J. Solid-State Circuits* **1974**, *9*, 256.
[13] M. B. Taylor, *IEEE Micro.* **2013**, *33*, 8.
[14] J. Backus, *Commun. ACM* **1978**, *21*, 613.
[15] J. D. Kendall, S. Kumar, *Appl. Phys. Rev.* **2020**, *7*, 029901.
[16] A. Calimera, E. Macii, M. Poncino, *Funct. Neurol.* **2013**, *28*, 191.
[17] S. K. Esser, P. A. Merolla, J. V. Arthur, A. S. Cassidy, R. Appuswamy, A. Andreopoulos, D. J. Berg, J. L. McKinstry, T. Melano, D. R. Barch, C. Di Nolfo, P. Datta, A. Amir, B. Taba, M. D. Flickner, D. S. Modha, *Proc. Natl. Acad. Sci. USA* **2016**, *113*, 11441.
[18] G. Csaba, W. Porod, *Appl. Phys. Rev.* **2020**, *7*, 011302.
[19] S. J. Kim, S. B. Kim, H. W. Jang, *iScience* **2021**, *24*, 101889.
[20] K. Amunts, C. Ebell, J. Muller, M. Telefont, A. Knoll, T. Lippert, *Neuron* **2016**, *92*, 574.
[21] E. J. Fuller, F. El Gabaly, F. Léonard, S. Agarwal, S. J. Plimpton, R. B. Jacobs-Gedrim, C. D. James, M. J. Marinella, A. A. Talin, *Adv. Mater.* **2017**, *29*, 1604310.
[22] C. Sen Yang, D. S. Shang, N. Liu, E. J. Fuller, S. Agrawal, A. A. Talin, Y. Q. Li, B. G. Shen, Y. Sun, *Adv. Funct. Mater.* **2018**, *28*, 1804170.
[23] P. A. Merolla, J. V. Arthur, R. Alvarez-icaza, A. S. Cassidy, J. Sawada, F. Akopyan, B. L. Jackson, N. Imam, C. Guo, Y. Nakamura, B. Brezzo, I. Vo, S. K. Esser, R. Appuswamy, B. Taba, A. Amir, M. D. Flickner, W. P. Risk, R. Manohar, D. S. Modha, *Science* **2014**, *345*, 668.
[24] N. Savage, *Commun. ACM* **2017**, *60*, 13.
[25] R. W. Keyes, *Rep. Prog. Phys.* **2005**, *68*, 2701.
[26] S. D. Ha, S. Ramanathan, *J. Appl. Phys.* **2011**, *110*, 071101.
[27] A. M. Ionescu, H. Riel, *Nature* **2011**, *479*, 329.
[28] Z. Yang, C. Ko, S. Ramanathan, *Annu. Rev. Mater. Res.* **2011**, *41*, 337.
[29] S. Kumar, X. Wang, J. P. Strachan, Y. Yang, W. D. Lu, *Nat. Rev. Mater.* **2022**, *7*, 575.
[30] M. D. Pickett, G. Medeiros-Ribeiro, R. S. Williams, *Nat. Mater.* **2013**, *12*, 114.
[31] M. D. Pickett, R. S. Williams, *Nanotechnology* **2012**, *23*, 215202.
[32] Z. Wang, M. Rao, J. W. Han, J. Zhang, P. Lin, Y. Li, C. Li, W. Song, S. Asapu, R. Midya, Y. Zhuo, H. Jiang, J. H. Yoon, N. K. Upadhyay, S. Joshi, M. Hu, J. P. Strachan, M. Barnell, Q. Wu, H. Wu, Q. Qiu, R. S. Williams, Q. Xia, J. J. Yang, *Nat. Commun.* **2018**, *9*, 3208.
[33] S. Kumar, J. P. Strachan, R. S. Williams, *Nature* **2017**, *548*, 318.
[34] T. J. Park, S. Deng, S. Manna, A. N. M. N. Islam, H. Yu, Y. Yuan, D. D. Fong, A. A. Chubykin, A. Sengupta, S. K. R. S. Sankaranarayanan, S. Ramanathan, *Adv. Mater.* **2022**, 2203352.
[35] S. Wall, S. Yang, L. Vidas, M. Chollet, J. M. Glownia, M. Kozina, T. Katayama, T. Henighan, M. Jiang, T. A. Miller, D. A. Reis, L. A. Boatner, O. Delaire, M. Trigo, *Science* **2018**, *362*, 572.
[36] W. H. Brito, M. C. O. Aguiar, K. Haule, G. Kotliar, *Phys. Rev. Lett.* **2016**, *117*, 056402.
[37] J. Del Valle, P. Salev, S. Gariglio, Y. Kalcheim, I. K. Schuller, J. M. Triscone, *Nano Lett.* **2022**, *22*, 1251.
[38] L. Whittaker, C. J. Patridge, S. Banerjee, *J. Phys. Chem. Lett.* **2011**, *2*, 745.
[39] W. Fan, J. Cao, J. Seidel, Y. Gu, J. W. Yim, C. Barrett, K. M. Yu, J. Ji, R. Ramesh, L. Q. Chen, J. Wu, *Phys. Rev. B: Condens. Matter Mater. Phys.* **2011**, *83*, 235102.
[40] E. J. Braham, D. Sellers, E. Emmons, R. Villarreal, H. Asayesh-Ardakani, N. A. Fleer, K. E. Farley, R. Shahbazian-Yassar, R. Arròyave, P. J. Shamberger, S. Banerjee, *Chem. Mater.* **2018**, *30*, 214.
[41] Y. G. Liang, S. Lee, H. S. Yu, H. R. Zhang, Y. J. Liang, P. Y. Zavalij, X. Chen, R. D. James, L. A. Bendersky, A. V. Davydov, X. H. Zhang, I. Takeuchi, *Nat. Commun.* **2020**, *11*, 3539.
[42] J. D. Budai, J. Hong, M. E. Manley, E. D. Specht, C. W. Li, J. Z. Tischler, D. L. Abernathy, A. H. Said, B. M. Leu, L. A. Boatner, R. J. McQueeney, O. Delaire, *Nature* **2014**, *515*, 535.
[43] Y. Cui, Y. Ke, C. Liu, Z. Chen, N. Wang, L. Zhang, Y. Zhou, S. Wang, Y. Gao, Y. Long, *Joule* **2018**, *2*, 1707.
[44] X. Cao, T. Chang, Z. Shao, F. Xu, H. Luo, P. Jin, *Matter* **2020**, *2*, 862.
[45] S. Lany, *J. Phys.: Condens. Matter* **2015**, *27*, 283203.
[46] S. Choi, A. Kutepov, K. Haule, M. van Schilfgaarde, G. Kotliar, *Nat. Commun.* **2016**, *1*, 16001.
[47] X. Yuan, Y. Zhang, T. A. Abtew, P. Zhang, W. Zhang, *Phys. Rev. B: Condens. Matter Mater. Phys.* **2012**, *86*, 235103.
[48] S. M. Bohaichuk, S. Kumar, G. Pitner, C. J. McClellan, J. Jeong, M. G. Samant, H. S. P. Wong, S. S. P. Parkin, R. S. Williams, E. Pop, *Nano Lett.* **2019**, *19*, 6751.
[49] S. Kumar, R. S. Williams, *Nat. Commun.* **2018**, *9*, 2030.
[50] B. K. Ridley, *Proc. Phys. Soc.* **1963**, *82*, 954.
[51] T. D. Brown, S. Kumar, R. S. Williams, *Appl. Phys. Rev.* **2022**, *9*, 011308.
[52] A. Ascoli, A. S. Demirkol, R. Tetzlaff, S. Slesazeck, T. Mikolajick, L. O. Chua, *Front. Neurosci.* **2021**, *15*, 651452.
[53] A. Ascoli, S. Slesazeck, H. Mähne, R. Tetzlaff, S. Member, T. Mikolajick, S. Member, *IEEE Trans. Circuits Syst. I: Regul. Pap.* **2015**, *62*, 1165.
[54] I. Messaris, T. D. Brown, A. S. Demirkol, A. Ascoli, M. M. Al Chawa, R. S. Williams, S. Member, R. Tetzlaff, S. Member, L. O. Chua, *IEEE Trans. Circuits Syst. I Regul. Pap.* **2021**, *68*, 4979.

© 2022 Wiley-VCH GmbH

[55] L. Chua, *IEEE Trans. Circuit Theory* **1971**, *CT-18*, 507.
[56] L. O. Chua, S. M. Kang, *Proc. IEEE* **1976**, *64*, 209.
[57] G. A. Gibson, *Adv. Funct. Mater.* **2018**, *28*, 1704175.
[58] A. S. Alexandrov, A. M. Bratkovsky, B. Bridle, S. E. Savel'Ev, D. B. Strukov, R. Stanley Williams, *Appl. Phys. Lett.* **2011**, *99*, 202104.
[59] L. O. Chua, *IEEE Trans. Circuits Syst. I: Fundam. Theory Appl.* **1999**, *46*, 71.
[60] A. Yano, H. Clarke, D. G. Sellers, E. J. Braham, T. E. G. Alivio, S. Banerjee, P. J. Shamberger, *J. Phys. Chem. C* **2020**, *124*, 21223.
[61] P. Schofield, E. J. Braham, B. Zhang, J. L. Andrews, H. K. Drozdick, D. Zhao, W. Zaheer, R. M. Gurrola, K. Xie, P. J. Shamberger, X. Qian, S. Banerjee, *Chem. Commun.* **2022**, *58*, 6586.
[62] D. Wegkamp, J. Stähler, *Prog. Surf. Sci.* **2015**, *90*, 464.
[63] D. Lee, B. Chung, Y. Shi, G. Kim, N. Campbell, F. Xue, K. Song, S. Choi, J. P. Podkaminer, T. H. Kim, P. J. Ryan, J. Kim, T. R. Paudel, J. Kang, J. W. Spinuzzi, D. A. Tenne, E. Y. Tsymbal, M. S. Rzchowski, L. Q. Chen, J. Lee, C. B. Eom, *Science* **2018**, *362*, 1037.
[64] J. Jeong, N. Aetukuri, T. Graf, T. D. Schladt, M. G. Samant, S. S. P. Parkin, *Science* **2013**, *339*, 1402.
[65] J. Park, C. Oh, J. Son, *J. Mater. Chem. C* **2021**, *9*, 2521.
[66] C. Oh, I. Kim, J. Park, Y. Park, M. Choi, J. Son, *Adv. Electron. Mater.* **2021**, *7*, 2000802.
[67] Z. Zhang, R. D. James, S. Müller, *Acta Mater.* **2009**, *57*, 4332.
[68] A. R. Balakrishna, *J. Electrochem. Energy Convers. Storage* **2022**, *19*, 040802.
[69] S. A. Howard, E. Evlyukhin, G. Páez Fajardo, H. Paik, D. G. Schlom, L. F. J. Piper, *Adv. Mater. Interfaces* **2021**, *8*, 2001790.
[70] N. F. Quackenbush, J. W. Tashman, J. A. Mundy, S. Sallis, H. Paik, R. Misra, J. A. Moyer, J. H. Guo, D. A. Fischer, J. C. Woicik, D. A. Muller, D. G. Schlom, L. F. J. Piper, *Nano Lett.* **2013**, *13*, 4857.
[71] B. M. Hudak, S. W. Depner, G. R. Waetzig, A. Talapatra, R. Arroyave, S. Banerjee, B. S. Guiton, *Nat. Commun.* **2017**, *8*, 15316.
[72] A. Parija, G. R. Waetzig, J. L. Andrews, S. Banerjee, *J. Phys. Chem. C* **2018**, *122*, 25709.
[73] A. Krammer, A. Magrez, W. A. Vitale, P. Mocny, P. Jeanneret, E. Guibert, H. J. Whitlow, A. M. Ionescu, A. Schüler, *J. Appl. Phys.* **2017**, *122*, 045304.
[74] D. G. Sellers, E. J. Braham, R. Villarreal, B. Zhang, A. Parija, T. D. Brown, T. E. G. Alivio, H. Clarke, L. R. De Jesus, L. Zuin, D. Prendergast, X. Qian, R. Arroyave, P. J. Shamberger, S. Banerjee, *J. Am. Chem. Soc.* **2020**, *142*, 15513.
[75] C. E. Wilson, A. E. Gibson, J. J. Argo, P. A. Loughney, W. Xu, G. King, V. Doan-Nguyen, *J. Mater. Res.* **2021**, *36*, 268.
[76] E. J. Braham, J. L. Andrews, T. E. G. Alivio, N. A. Fleer, S. Banerjee, *Phys. Status Solidi A* **2018**, *215*, 1700884.
[77] M. Marezio, D. B. McWhan, J. P. Remeika, P. D. Dernier, *Phys. Rev. B* **1972**, *5*, 2541.
[78] A. Zylbersztejn, N. F. Mott, *Phys. Rev. B* **1975**, *11*, 4383.
[79] A. Tselev, I. A. Luk'Yanchuk, I. N. Ivanov, J. D. Budai, J. Z. Tischler, E. Strelcov, A. Kolmakov, S. V. Kalinin, *Nano Lett.* **2010**, *10*, 4409.
[80] J. L. Victor, M. Gaudon, G. Salvatori, O. Toulemonde, N. Penin, A. Rougier, *J. Phys. Chem. Lett.* **2021**, *12*, 7792.
[81] Y. Filinchuk, N. A. Tumanov, V. Ban, H. Ji, J. Wei, M. W. Swift, A. H. Nevidomskyy, D. Natelson, *J. Am. Chem. Soc.* **2014**, *136*, 8100.
[82] C. H. Griffiths, H. K. Eastwood, *J. Appl. Phys.* **1974**, *45*, 2201.
[83] D. Ruzmetov, S. D. Senanayake, V. Narayanamurti, S. Ramanathan, *Phys. Rev. B* **2008**, *77*, 195442.
[84] J. Montero, Y.-X. Ji, S.-Y. Li, G. A. Niklasson, C. G. Granqvist, *J. Vac. Sci. Technol., B: Nanotechnol. Microelectron.: Mater. Process., Meas., Phenom.* **2015**, *33*, 031805.
[85] G. A. Horrocks, S. Singh, M. F. Likely, G. Sambandamurthy, S. Banerjee, *ACS Appl. Mater. Interfaces* **2014**, *6*, 15726.
[86] K. Post, R. G. Robins, *Electrochim. Acta* **1976**, *21*, 401.
[87] T. E. G. Alivio, D. G. Sellers, H. Asayesh-Ardakani, E. J. Braham, G. A. Horrocks, K. E. Pelcher, R. Villareal, L. Zuin, P. J. Shamberger, R. Arroyave, R. Shahbazian-Yassar, S. Banerjee, *Chem. Mater.* **2017**, *29*, 5401.
[88] C. J. Patridge, L. Whittaker, B. Ravel, S. Banerjee, *J. Phys. Chem. C* **2012**, *116*, 3728.
[89] J. Du, Y. Gao, H. Luo, L. Kang, Z. Zhang, Z. Chen, C. Cao, *Sol. Energy Mater. Sol. Cells* **2011**, *95*, 469.
[90] H. Futaki, M. Aoki, Hisao Futaki, Minoru Aoki, *Jpn. J. Appl. Phys.* **1969**, *8*, 1008.
[91] L. Whittaker, T.-L. Wu, C. J. Patridge, G. Sambandamurthy, S. Banerjee, *J. Mater. Chem.* **2011**, *21*, 5580.
[92] S. J. Liu, H. W. Fang, Y. T. Su, J. H. Hsieh, *Jpn. J. Appl. Phys.* **2014**, *53*, 063201.
[93] W. Lu, G. Zhao, B. Song, J. Li, X. Zhang, G. Han, *Surf. Coat. Technol.* **2017**, *320*, 311.
[94] C. Piccirillo, R. Binions, I. P. Parkin, *Eur. J. Inorg. Chem.* **2007**, *2007*, 4050.
[95] A. Krammer, O. Bouvard, A. Schüler, *Energy Procedia* **2017**, *122*, 745.
[96] Y. Gao, C. Cao, L. Dai, H. Luo, M. Kanehira, Y. Ding, Z. L. Wang, *Energy Environ. Sci.* **2012**, *5*, 8708.
[97] W. Burkhardt, T. Christmann, B. K. Meyer, W. Niessner, D. Schalch, A. Scharmann, *Thin Solid Films* **1999**, *345*, 229.
[98] L. Dai, S. Chen, J. Liu, Y. Gao, J. Zhou, Z. Chen, C. Cao, H. Luo, M. Kanehira, *Phys. Chem. Chem. Phys.* **2013**, *15*, 11723.
[99] I. Top, J. Schläfer, R. Binions, I. Papakonstantinou, S. Srimuragananthan, M. Powell, I. Parkin, C. J. Carmalt, I. Abrahams, *MRS Adv.* **2018**, *3*, 1863.
[100] Y. Cui, Y. Wang, B. Liu, H. Luo, Y. Gao, *RSC Adv.* **2016**, *6*, 64394.
[101] M. Wan, M. Xiong, N. Li, B. Liu, S. Wang, W. Y. Ching, X. Zhao, *Appl. Surf. Sci.* **2017**, *410*, 363.
[102] K. Kawatani, T. Kanki, H. Tanaka, *Phys. Rev. B: Condens. Matter Mater. Phys.* **2014**, *90*, 054203.
[103] P. Baum, D. S. Yang, A. H. Zewail, *Springer Ser. Chem. Phys.* **2009**, *92*, 116.
[104] H. Clarke, B. D. Caraway, D. G. Sellers, E. J. Braham, S. Banerjee, R. Arróyave, P. J. Shamberger, *Phys. Rev. Mater.* **2018**, *2*, 103402.
[105] J. Zhou, Y. Gao, X. Liu, Z. Chen, L. Dai, C. Cao, H. Luo, M. Kanahira, C. Sun, L. Yan, *Phys. Chem. Chem. Phys.* **2013**, *15*, 7505.
[106] F. Béteille, R. Morineau, J. Livage, M. Nagano, *Mater. Res. Bull.* **1997**, *32*, 1109.
[107] S. Chen, J. Liu, L. Wang, H. Luo, Y. Gao, *J. Phys. Chem. C* **2014**, *118*, 18938.
[108] E. Cavanna, J. P. Segaud, J. Livage, *Mater. Res. Bull.* **1999**, *34*, 167.
[109] Y. Wu, L. Fan, Q. Liu, S. Chen, W. Huang, F. Chen, G. Liao, C. Zou, Z. Wu, *Sci. Rep.* **2015**, *5*, 9328.
[110] R. Lopez, L. A. Boatner, T. E. Haynes, L. C. Feldman, R. F. Haglund, *J. Appl. Phys.* **2002**, *92*, 4031.
[111] L. Whittaker, C. Jaye, Z. Fu, D. A. Fischer, S. Banerjee, *J. Am. Chem. Soc.* **2009**, *131*, 8884.
[112] H. Asayesh-Ardakani, W. Yao, A. Nie, P. M. Marley, E. Braham, R. F. Klie, S. Banerjee, R. Shahbazian-Yassar, *Appl. Phys. Lett.* **2017**, *109*, 233104.
[113] K. Miyazaki, K. Shibuya, M. Suzuki, H. Wado, A. Sawa, *Jpn. J. Appl. Phys.* **2014**, *53*, 071102.
[114] M. K. Dietrich, F. Kuhl, A. Polity, P. J. Klar, *Appl. Phys. Lett.* **2017**, *110*, 141907.
[115] K. Miyazaki, K. Shibuya, M. Suzuki, K. Sakai, J.-I. Fujita, A. Sawa, *AIP Adv.* **2016**, *6*, 55012.
[116] C. Ji, Z. Wu, L. Lu, X. Wu, J. Wang, X. Liu, H. Zhou, Z. Huang, J. Gou, Y. Jiang, *J. Mater. Chem. C* **2018**, *6*, 6502.
[117] Y. Shi, L.-Q. Chen, ArXiv **2020**, *arXiv:2001.02264v1*.

 © 2022 Wiley-VCH GmbH

15214095, 2023, 37, Downloaded from https://onlinelibrary.wiley.com/doi/10.1002/adma.202205294 by Texas A&M University Library, Wiley Online Library on [06/12/2023]. See the Terms and Conditions (https://onlinelibrary.wiley.com/terms-and-conditions) on Wiley Online Library for rules of use; OA articles are governed by the applicable Creative Commons License

[118] Y. Shi, F. Xue, L.-Q. Chen, *EPL* **2017**, *120*, 46003.
[119] N. I. Cool, D. G. Sellers, M. Al-Hashimi, S. Banerjee, *ACS Appl. Energy Mater.* **2022**, *5*, 4829.
[120] J. Nag, R. F. Haglund, *J. Phys.: Condens. Matter* **2008**, *20*, 264016.
[121] K. Nagashima, T. Yanagida, H. Tanaka, T. Kawai, *J. Appl. Phys.* **2007**, *101*, 026103.
[122] R. E. Marvel, R. R. Harl, V. Craciun, B. R. Rogers, R. F. Haglund, *Acta Mater.* **2015**, *91*, 217.
[123] J. Narayan, V. M. Bhosle, *J. Appl. Phys.* **2006**, *100*, 103524.
[124] J. Cao, E. Ertekin, V. Srinivasan, W. Fan, S. Huang, H. Zheng, J. W. L. Yim, D. R. Khanal, D. F. Ogletree, J. C. Grossman, J. Wu, *Nat. Nanotechnol.* **2009**, *4*, 732.
[125] J. Wu, Q. Gu, B. S. Guiton, N. P. De Leon, L. Ouyang, H. Park, *Nano Lett.* **2006**, *6*, 2313.
[126] J. Yoon, H. Kim, X. Chen, N. Tamura, B. S. Mun, C. Park, H. Ju, *ACS Appl. Mater. Interfaces* **2016**, *8*, 2280.
[127] A. C. Jones, S. Berweger, J. Wei, D. Cobden, M. B. Raschke, *Nano Lett.* **2010**, *10*, 1574.
[128] A. Frenzel, M. M. Qazilbash, M. Brehm, B.-G. Chae, B.-J. Kim, H.-T. Kim, A. V. Balatsky, F. Keilmann, D. N. Basov, *Phys. Rev. B: Condens. Matter Mater. Phys.* **2009**, *80*, 115115.
[129] J. H. Park, J. M. Coy, T. Serkan Kasirga, C. Huang, Z. Fei, S. Hunter, D. H. Cobden, *Nature* **2013**, *500*, 431.
[130] B. Lazarovits, K. Kim, K. Haule, G. Kotliar, *Phys. Rev. B: Condens. Matter Mater. Phys.* **2010**, *81*, 115117.
[131] Y. Muraoka, Z. Hiroi, *Appl. Phys. Lett.* **2002**, *80*, 583.
[132] N. F. Quackenbush, H. Paik, M. J. Wahila, S. Sallis, M. E. Holtz, X. Huang, A. Ganose, B. J. Morgan, D. O. Scanlon, Y. Gu, F. Xue, L. Q. Chen, G. E. Sterbinsky, C. Schlueter, T. L. Lee, J. C. Woicik, J. H. Guo, J. D. Brock, D. A. Muller, D. A. Arena, D. G. Schlom, L. F. J. Piper, *Phys. Rev. B* **2016**, *94*, 085105.
[133] N. B. Aetukuri, A. X. Gray, M. Drouard, M. Cossale, L. Gao, A. H. Reid, R. Kukreja, H. Ohldag, C. A. Jenkins, E. Arenholz, K. P. Roche, H. A. Dürr, M. G. Samant, S. S. P. Parkin, *Nat. Phys.* **2013**, *9*, 661.
[134] M. M. Qazilbash, M. Brehm, G. O. Andreev, A. Frenzel, P. C. Ho, B. G. Chae, B. J. Kim, S. J. Yun, H. T. Kim, A. V. Balatsky, O. G. Shpyrko, M. B. Maple, F. Keilmann, D. N. Basov, *Phys. Rev. B: Condens. Matter Mater. Phys.* **2009**, *79*, 075107.
[135] J. Jian, A. Chen, Y. Chen, X. Zhang, H. Wang, *Appl. Phys. Lett.* **2017**, *111*, 153102.
[136] M. K. Liu, M. Wagner, E. Abreu, S. Kittiwatanakul, A. McLeod, Z. Fei, M. Goldflam, S. Dai, M. M. Fogler, J. Lu, S. A. Wolf, R. D. Averitt, D. N. Basov, *Phys. Rev. Lett.* **2013**, *111*, 96602.
[137] Y. Zhao, J. Hwan Lee, Y. Zhu, M. Nazari, C. Chen, H. Wang, A. Bernussi, M. Holtz, Z. Fan, *J. Appl. Phys.* **2012**, *111*, 053533.
[138] G. Xu, P. Jin, M. Tazawa, K. Yoshimura, *Appl. Surf. Sci.* **2005**, *244*, 449.
[139] J. Li, J. Dho, *J. Cryst. Growth* **2014**, *404*, 84.
[140] K. Nagashima, T. Yanagida, H. Tanaka, T. Kawai, *Phys. Rev. B: Condens. Matter Mater. Phys.* **2006**, *74*, 13.
[141] H. Paik, J. A. Moyer, T. Spila, J. W. Tashman, J. A. Mundy, E. Freeman, N. Shukla, J. M. Lapano, R. Engel-Herbert, W. Zander, J. Schubert, D. A. Muller, S. Datta, P. Schiffer, D. G. Schlom, *Appl. Phys. Lett.* **2015**, *107*, 163101.
[142] L. L. Fan, S. Chen, Z. L. Luo, Q. H. Liu, Y. F. Wu, L. Song, D. X. Ji, P. Wang, W. S. Chu, C. Gao, C. W. Zou, Z. Y. Wu, *Nano Lett.* **2014**, *14*, 4036.
[143] A. Gupta, J. Narayan, T. Dutta, *Appl. Phys. Lett.* **2010**, *97*, 151912.
[144] D. Lee, J. Lee, K. Song, F. Xue, S. Y. Choi, Y. Ma, J. Podkaminer, D. Liu, S. C. Liu, B. Chung, W. Fan, S. J. Cho, W. Zhou, J. Lee, L. Q. Chen, S. H. Oh, Z. Ma, C. B. Eom, *Nano Lett.* **2017**, *17*, 5614.
[145] M. R. Bayati, R. Molaei, F. Wu, J. D. Budai, Y. Liu, R. J. Narayan, J. Narayan, *Acta Mater.* **2013**, *61*, 7805.
[146] J. Li, J. Dho, *J. Cryst. Growth* **2010**, *312*, 3287.
[147] E. Breckenfeld, H. Kim, K. Burgess, N. Charipar, S. F. Cheng, R. Stroud, A. Pique, *ACS Appl. Mater. Interfaces* **2017**, *9*, 1577.
[148] Y. Muraoka, K. Saeki, R. Eguchi, T. Wakita, M. Hirai, T. Yokoya, S. Shin, *J. Appl. Phys.* **2011**, *109*, 043702.
[149] M. Liu, M. Wagner, J. Zhang, A. McLeod, S. Kittiwatanakul, Z. Fei, E. Abreu, M. Goldflam, A. J. Sternbach, S. Dai, K. G. West, J. Lu, S. A. Wolf, R. D. Averitt, D. N. Basov, *Appl. Phys. Lett.* **2014**, *104*, 121905.
[150] M. Liu, A. J. Sternbach, M. Wagner, T. V. Slusar, T. Kong, S. L. Bud'ko, S. Kittiwatanakul, M. M. Qazilbash, A. McLeod, Z. Fei, E. Abreu, J. Zhang, M. Goldflam, S. Dai, G. X. Ni, J. Lu, H. A. Bechtel, M. C. Martin, M. B. Raschke, R. D. Averitt, S. A. Wolf, H. T. Kim, P. C. Canfield, D. N. Basov, *Phys. Rev. B: Condens. Matter Mater. Phys.* **2015**, *91*, 245155.
[151] M. Liu, A. J. Sternbach, D. N. Basov, *Rep. Prog. Phys.* **2017**, *80*, 014501.
[152] E. Abreu, M. Liu, J. Lu, K. G. West, S. Kittiwatanakul, W. Yin, S. A. Wolf, R. D. Averitt, *New J. Phys.* **2012**, *14*, 083026.
[153] C. B. Greenberg, *Thin Solid Films* **1983**, *110*, 73.
[154] P. Jin, S. Tanemura, *Thin Solid Films* **1996**, *281–282*, 239.
[155] P. Jin, S. Tanemura, *Jpn. J. Appl. Phys.* **1995**, *34*, 2459.
[156] P. Jin, S. Nakao, S. Tanemura, *Thin Solid Films* **1998**, *324*, 151.
[157] Z. P. Wu, A. Miyashita, S. Yamamoto, H. Abe, I. Nashiyama, K. Narumi, H. Naramoto, *J. Appl. Phys.* **1999**, *86*, 5311.
[158] J. C. Lee, G. V. Jorgenson, *Sol. Energy Mater.* **1986**, *14*, 205.
[159] P. Jin, S. Nakao, S. Tanemura, *Nucl. Instrum. Methods Phys. Res., Sect. B* **1998**, *141*, 419.
[160] A. Paone, R. Sanjines, P. Jeanneret, H. J. Whitlow, E. Guibert, G. Guibert, F. Bussy, J. L. Scartezzini, A. Schüler, *J. Alloys Compd.* **2015**, *621*, 206.
[161] K. A. Khan, G. A. Niklasson, C. G. Granqvist, *J. Appl. Phys.* **1988**, *64*, 3327.
[162] H. Yoon, M. Choi, T. W. Lim, H. Kwon, K. Ihm, J. K. Kim, S. Y. Choi, J. Son, *Nat. Mater.* **2016**, *15*, 1113.
[163] A. Krammer, A. Gremaud, O. Bouvard, R. Sanjines, A. Schüler, *Surf. Interface Anal.* **2016**, *48*, 440.
[164] I. Balberg, B. Abeles, Y. Arie, *Thin Solid Films* **1974**, *24*, 307.
[165] J. Livage, F. Béteille, J. Livage, *J. Sol-Gel Sci. Technol.* **1998**, *13*, 65.
[166] P. Jin, M. Tazawa, M. Ikeyama, S. Tanemura, K. Macák, X. Wang, S. Olafsson, U. Helmersson, *J. Vac. Sci. Technol., A* **1999**, *17*, 1817.
[167] K. Shibuya, M. Kawasaki, Y. Tokura, *Appl. Phys. Lett.* **2010**, *96*, 022102.
[168] M. Zhu, H. Wang, B. Wang, H. Qi, D. Zhang, W. Lv, *Ceram. Int.* **2019**, *45*, 1661.
[169] I. G. Madiba, N. Émond, M. Chaker, F. T. Thema, S. I. Tadadjeu, U. Muller, P. Zolliker, A. Braun, L. Kotsedi, M. Maaza, *Appl. Surf. Sci.* **2017**, *411*, 271.
[170] I. G. Madiba, N. Émond, M. Chaker, B. S. Khanyile, S. I. Tadadjeu, P. Zolliker, M. Izerrouken, N. Matinise, A. Braun, M. Nkosi, M. Maaza, *Nucl. Instrum. Methods Phys. Res., Sect. B* **2019**, *443*, 25.
[171] A. Leone, A. M. Trione, F. Junga, *IEEE Trans. Nucl. Sci.* **1990**, *37*, 1739.
[172] W. M. Tong, J. J. Yang, P. J. Kuekes, D. R. Stewart, R. S. Williams, E. DeIonno, E. E. King, S. C. Witczak, M. D. Looper, J. V. Osborn, *IEEE Trans. Nucl. Sci.* **2010**, *57*, 1640.
[173] T. Yajima, Y. Ninomiya, T. Nishimura, A. Toriumi, *Phys. Rev. B: Condens. Matter Mater. Phys.* **2015**, *91*, 205102.
[174] L. Rodríguez, E. Del Corro, M. Conroy, K. Moore, F. Sandiumenge, N. Domingo, J. Santiso, G. Catalan, *ACS Appl. Electron. Mater.* **2020**, *2*, 1433.
[175] J. Cao, Y. Gu, W. Fan, L. Q. Chen, D. F. Ogletree, K. Chen, N. Tamura, M. Kunz, C. Barrett, J. Seidel, J. Wu, *Nano Lett.* **2010**, *10*, 2667.

© 2022 Wiley-VCH GmbH

15214095, 2023, 37, Downloaded from https://onlinelibrary.wiley.com/doi/10.1002/adma.202205294 by Texas A&M University Library, Wiley Online Library on [06/12/2023]. See the Terms and Conditions (https://onlinelibrary.wiley.com/terms-and-conditions) on Wiley Online Library for rules of use; OA articles are governed by the applicable Creative Commons License

[176] P. Jin, S. Nakao, S. Tanemura, T. Bell, L. S. Wielunski, M. V. Swain, *Thin Solid Films* **1999**, *343–344*, 134.
[177] A. Rúa, R. Cabrera, H. Coy, E. Merced, N. Sepúlveda, F. E. Fernández, *J. Appl. Phys.* **2012**, *111*, 104502.
[178] H. Guo, K. Chen, Y. Oh, K. Wang, C. Dejoie, S. A. Syed Asif, O. L. Warren, Z. W. Shan, J. Wu, A. M. Minor, *Nano Lett.* **2011**, *11*, 3207.
[179] D. Singh, B. Viswanath, *J. Mater. Sci.* **2017**, *52*, 5589.
[180] J. Hay, B. Crawford, *J. Mater. Res.* **2011**, *26*, 727.
[181] B. Viswanath, C. Ko, S. Ramanathan, *Scr. Mater.* **2011**, *64*, 490.
[182] F. Sandiumenge, L. Rodríguez, M. Pruneda, C. Magén, J. Santiso, G. Catalan, *Adv. Mater.* **2021**, *33*, 2004374.
[183] J. O. Krisponeit, S. Fischer, S. Esser, V. Moshnyaga, T. Schmidt, L. F. J. Piper, J. I. Flege, J. Falta, *Sci. Rep.* **2020**, *10*, 22374.
[184] Y. Yang, X. Mao, Y. Yao, H. Huang, Y. Lu, L. Luo, X. Zhang, G. Yin, T. Yang, X. Gao, *J. Appl. Phys.* **2019**, *125*, 082508.
[185] H. T. Kim, B. G. Chae, D. H. Youn, G. Kim, K. Y. Kang, S. J. Lee, K. Kim, Y. S. Lim, *Appl. Phys. Lett.* **2005**, *86*, 242101.
[186] A. Joushaghani, J. Jeong, S. Paradis, D. Alain, J. Stewart Aitchison, J. K. S. Poon, *Appl. Phys. Lett.* **2014**, *104*, 221904.
[187] T. Driscoll, J. Quinn, M. Di Ventra, D. N. Basov, G. Seo, Y. W. Lee, H. T. Kim, D. R. Smith, *Phys. Rev. B: Condens. Matter Mater. Phys.* **2012**, *86*, 094203.
[188] D. Ruzmetov, G. Gopalakrishnan, J. Deng, V. Narayanamurti, S. Ramanathan, *J. Appl. Phys.* **2009**, *106*, 083702.
[189] D. Gu, H. Qin, X. Zhou, S. Xu, Y. Jiang, *AIP Adv.* **2018**, *8*, 015317.
[190] S. B. Lee, K. Kim, J. S. Oh, B. Kahng, J. S. Lee, *Appl. Phys. Lett.* **2013**, *102*, 063501.
[191] D. Li, A. A. Sharma, D. K. Gala, N. Shukla, H. Paik, S. Datta, D. G. Schlom, J. A. Bain, M. Skowronski, *ACS Appl. Mater. Interfaces* **2016**, *8*, 12908.
[192] G. M. Liao, S. Chen, L. L. Fan, Y. L. Chen, X. Q. Wang, H. Ren, Z. M. Zhang, C. W. Zou, *AIP Adv.* **2016**, *6*, 045014.
[193] I. P. Radu, B. Govoreanu, S. Mertens, X. Shi, M. Cantoro, M. Schaekers, M. Jurczak, S. De Gendt, A. Stesmans, J. A. Kittl, M. Heyns, K. Martens, *Nanotechnology* **2015**, *26*, 165202.
[194] A. Zimmers, L. Aigouy, M. Mortier, A. Sharoni, S. Wang, K. G. West, J. G. Ramirez, I. K. Schuller, *Phys. Rev. Lett.* **2013**, *110*, 056601.
[195] B. Simon Mun, J. Yoon, S. K. Mo, K. Chen, N. Tamura, C. Dejoie, M. Kunz, Z. Liu, C. Park, K. Moon, H. Ju, *Appl. Phys. Lett.* **2013**, *103*, 061902.
[196] J. Yoon, G. Lee, C. Park, B. S. Mun, H. Ju, *Appl. Phys. Lett.* **2014**, *105*, 083503.
[197] S. Kumar, M. D. Pickett, J. P. Strachan, G. Gibson, Y. Nishi, R. S. Williams, *Adv. Mater.* **2013**, *25*, 6128.
[198] K. Okimura, N. Ezreena, Y. Sasakawa, J. Sakai, *Jpn. J. Appl. Phys.* **2009**, *48*, 065003.
[199] J. Kim, C. Ko, A. Frenzel, S. Ramanathan, J. E. Hoffman, *Appl. Phys. Lett.* **2010**, *96*, 213106.
[200] E. Freeman, G. Stone, N. Shukla, H. Paik, J. A. Moyer, Z. Cai, H. Wen, R. Engel-Herbert, D. G. Schlom, V. Gopalan, S. Datta, *Appl. Phys. Lett.* **2013**, *103*, 263109.
[201] J. Duchene, M. Terraillon, P. Pailly, G. Adam, *Appl. Phys. Lett.* **1971**, *19*, 115.
[202] J. Yoon, H. Kim, B. S. Mun, C. Park, H. Ju, *J. Appl. Phys.* **2016**, *119*, 124503.
[203] B. G. Chae, H. T. Kim, D. H. Youn, K. Y. Kang, *Phys. B: Condens. Matter* **2005**, *369*, 76.
[204] Y. Zhou, X. Chen, C. Ko, Z. Yang, C. Mouli, S. Ramanathan, *IEEE Electron Device Lett.* **2013**, *34*, 220.
[205] J. Leroy, A. Crunteanu, A. Bessaudou, F. Cosset, C. Champeaux, J. C. Orlianges, *Appl. Phys. Lett.* **2012**, *100*, 213507.
[206] W. Xue, G. Liu, Z. Zhong, Y. Dai, J. Shang, Y. Liu, H. Yang, X. Yi, H. Tan, L. Pan, S. Gao, J. Ding, X. H. Xu, R. W. Li, *Adv. Mater.* **2017**, *29*, 1702162.
[207] B. Hu, Y. Ding, W. Chen, D. Kulkarni, Y. Shen, V. V. Tsukruk, Z. L. Wang, *Adv. Mater.* **2010**, *22*, 5134.
[208] B. Fisher, *J. Phys. C: Solid State Phys.* **1975**, *8*, 2072.
[209] T. L. Wu, L. Whittaker, S. Banerjee, G. Sambandamurthy, *Phys. Rev. B: Condens. Matter Mater. Phys.* **2011**, *83*, 2.
[210] Z. Zhao, J. Li, C. Ling, X. Zhao, Y. Zhao, H. Jin, *Thin Solid Films* **2021**, *725*, 138643.
[211] Z. Zou, Z. Zhang, J. Xu, Z. Yu, M. Cheng, R. Xiong, Z. Lu, Y. Liu, J. Shi, *J. Alloys Compd.* **2019**, *806*, 310.
[212] A. Bradicich, H. Clarke, E. J. Braham, A. Yano, D. Sellers, S. Banerjee, P. J. Shamberger, *Adv. Electron. Mater.* **2021**, *8*, 2100932.
[213] K. Ito, K. Nishikawa, H. Iizuka, *Appl. Phys. Lett.* **2016**, *108*, 053507.
[214] S. H. Bae, S. Lee, H. Koo, L. Lin, B. H. Jo, C. Park, Z. L. Wang, *Adv. Mater.* **2013**, *25*, 5098.
[215] Y. Jung, J. Jeong, Z. Qu, B. Cui, A. Khanda, S. S. P. Parkin, J. K. S. Poon, *Adv. Electron. Mater.* **2021**, *7*, 2001142.
[216] S. Singh, T. A. Abtew, G. Horrocks, C. Kilcoyne, P. M. Marley, A. A. Stabile, S. Banerjee, P. Zhang, G. Sambandamurthy, *Phys. Rev. B* **2016**, *93*, 125132.
[217] B. Zhi, G. Gao, H. Xu, F. Chen, X. Tan, P. Chen, L. Wang, W. Wu, *ACS Appl. Mater. Interfaces* **2014**, *6*, 4603.
[218] H. Bian, Y. Y. Goh, Y. Liu, H. Ling, L. Xie, X. Liu, *Adv. Mater.* **2021**, *33*, 1.
[219] X. Deng, S. Q. Wang, Y. X. Liu, N. Zhong, Y. H. He, H. Peng, P. H. Xiang, C. G. Duan, *Adv. Funct. Mater.* **2021**, *31*, 2101099.
[220] Z. Tian, B. Xu, B. Hsu, L. Stan, Z. Yang, Y. Mei, *Nano Lett.* **2018**, *18*, 3017.
[221] L. Shan, Z. Wang, L. Bao, S. Bao, Y. Qin, Y. Ling, G. Bai, J. Robertson, Y. Cai, R. Huang, *Adv. Intell. Syst.* **2022**, *2100264*, 2100264.
[222] W. Wei, T. Huang, S. Wang, W. Luo, T. Zhang, W. Hu, X. Chen, N. Dai, *Phys. Status Solidi RRL* **2019**, *13*, 1900383.
[223] A. Joushaghani, J. Jeong, S. Paradis, D. Alain, J. Stewart Aitchison, J. K. S. Poon, *Appl. Phys. Lett.* **2014**, *105*, 231904.
[224] E. Goi, Q. Zhang, X. Chen, H. Luan, M. Gu, *PhotoniX* **2020**, *1*, 3.
[225] M. F. Jager, C. Ott, P. M. Kraus, C. J. Kaplan, W. Pouse, R. E. Marvel, R. F. Haglund, D. M. Neumark, S. R. Leone, *Proc. Natl. Acad. Sci. USA* **2017**, *114*, 9558.
[226] V. R. Morrison, R. P. Chatelain, K. L. Tiwari, A. Hendaoui, A. Bruhács, M. Chaker, B. J. Siwick, *Science* **2014**, *346*, 445.
[227] B. T. O'Callahan, A. C. Jones, J. Hyung Park, D. H. Cobden, J. M. Atkin, M. B. Raschke, *Nat. Commun.* **2015**, *6*, 6849.
[228] S. A. Dönges, O. Khatib, B. T. O'Callahan, J. M. Atkin, J. H. Park, D. Cobden, M. B. Raschke, *Nano Lett.* **2016**, *16*, 3029.
[229] K. A. Hallman, K. J. Miller, A. Baydin, S. M. Weiss, R. F. Haglund, *Adv. Opt. Mater.* **2021**, *9*, 2001721.
[230] Y. Jung, H. Han, A. Sharma, J. Jeong, S. S. P. Parkin, J. K. S. Poon, *ACS Photonics* **2022**, *9*, 217.
[231] T. Kang, Z. Ma, J. Qin, Z. Peng, W. Yang, T. Huang, S. Xian, S. Xia, W. Yan, Y. Yang, Z. Sheng, J. Shen, C. Li, L. Deng, L. Bi, *Nanophotonics* **2020**, *10*, 909.
[232] X. Zhou, L. Xhao, W. Zhen, Y. Lin, C. Wang, T. Pan, L. Li, G. Du, L. Lu, X. Cao, D. Li, *Adv. Electron. Mater.* **2021**, *7*, 2001254.
[233] H. Luo, B. Wang, E. Wang, X. Wang, Y. Sun, Q. Li, S. Fan, C. Cheng, K. Liu, *Appl. Phys. Rev.* **2019**, *6*, 041407.
[234] E. Corti, A. Khanna, K. Niang, J. Robertson, K. E. Moselund, B. Gotsmann, S. Datta, S. Karg, *IEEE Electron Device Lett.* **2020**, *41*, 629.
[235] R. Yuan, Q. Duan, P. J. Tiw, L. Ge, Z. Xiao, Z. Jing, K. Yang, C. Liu, C. Ge, R. Huang, Y. Yang, *Nat. Commun.* **2022**, *13*, 3973.
[236] S. Kumar, R. S. Williams, Z. Wang, *Nature* **2020**, *585*, 518.
[237] M. A. Nahmias, T. F. De Lima, A. N. Tait, H. T. Peng, B. J. Shastri, P. R. Prucnal, *IEEE J. Sel. Top. Quantum Electron.* **2020**, *26*, 7701518.

© 2022 Wiley-VCH GmbH

15214095, 2023, 37, Downloaded from https://onlinelibrary.wiley.com/doi/10.1002/adma.202205294 by Texas A&M University Library, Wiley Online Library on [06/12/2023]. See the Terms and Conditions (https://onlinelibrary.wiley.com/terms-and-conditions) on Wiley Online Library for rules of use; OA articles are governed by the applicable Creative Commons License

[238] D. V Christensen, R. Dittmann, B. Linares-Barranco, A. Sebastian, M. Le Gallo, A. Redaelli, S. Slesazeck, T. Mikolajick, S. Spiga, S. Menzel, I. Valov, G. Milano, C. Ricciardi, S.-J. Liang, F. Miao, M. Lanza, T. J. Quill, S. T. Keene, A. Salleo, J. Grollier, D. Marković, A. Mizrahi, P. Yao, J. J. Yang, G. Indiveri, J. P. Strachan, S. Datta, E. Vianello, A. Valentian, J. Feldmann, et al., *Neuromorphic Comput. Eng.* **2022**, *2*, 022501.
[239] I. Bendixson, *Acta Math.* **1901**, *24*, 1.
[240] J. V. Handy, W. Zaheer, A. R. M. Rothfuss, C. R. McGranahan, G. Agbeworvi, J. L. Andrews, K. E. García-Pedraza, J. D. Ponis, J. R. Ayala, Y. Ding, D. F. Watson, S. Banerjee, *Chem. Mater.* **2022**, *34*, 1439.
[241] A. Parija, J. V. Handy, J. L. Andrews, J. Wu, L. Wangoh, S. Singh, C. Jozwiak, A. Bostwick, E. Rotenberg, W. Yang, S. C. Fakra, M. Al-Hashimi, G. Sambandamurthy, L. F. J. Piper, R. S. Williams, D. Prendergast, S. Banerjee, *Matter* **2020**, *2*, 1166.
[242] Y. Luo, S. Rezaei, D. Santos, Y. Zhang, J. V. Handy, L. Carrillo, B. J. Schultz, L. Gobbato, M. Pupucevski, K. Wiaderek, H. Charalambous, A. Yakovenko, M. Pharr, B.-X. Xu, S. Banerjee, *Proc. Natl. Acad. Sci. USA* **2022**, *119*, 2115072119.
[243] J. L. Andrews, P. Stein, D. A. Santos, C. J. Chalker, L. R. De Jesus, R. D. Davidson, M. A. Gross, M. Pharr, J. D. Batteas, B.-X. Xu, S. Banerjee, **2020**, *Matter*, *3*, 1754.

Parker Schofield is a fifth-year Chemistry doctoral student advised by Sarbajit Banerjee at Texas A&M University. He earned his undergraduate degrees in Chemistry and English from Utah State University in 2018. His research interests pertain broadly to electrochemical energy storage, neuromorphic computing materials design, and doping in phase-transition materials.

Adelaide Bradicich is currently pursuing her Ph.D. in Materials Science and Engineering at Texas A&M University. Under the supervision of Dr. Patrick Shamberger, her research focuses on the development and characterization of vanadium dioxide devices, as well as modeling the electrical and thermal behavior of that material under an electrical bias. She earned her B.S. in Chemistry and Physics from Texas A&M University – Commerce.

Rebeca M. Gurrola is currently pursuing her Ph.D. in Materials Science and Engineering at Texas A&M University. Under the supervision of Dr. Patrick Shamberger, her research focuses on synthesis and characterization of vanadium dioxide thin film systems as well as defect engineering of VO_2 for neuromorphic applications. She earned her B.S. in Physics and B.A. in Mathematics from St. Mary's University.

© 2022 Wiley-VCH GmbH

15214095, 2023, 37, Downloaded from https://onlinelibrary.wiley.com/doi/10.1002/adma.202205294 by Texas A&M University Library, Wiley Online Library on [06/12/2023]. See the Terms and Conditions (https://onlinelibrary.wiley.com/terms-and-conditions) on Wiley Online Library for rules of use; OA articles are governed by the applicable Creative Commons License

15214095, 2023, 37, Downloaded from https://onlinelibrary.wiley.com/doi/10.1002/adma.202205294 by Texas A&M University Library, Wiley Online Library on [06/12/2023]. See the Terms and Conditions (https://onlinelibrary.wiley.com/terms-and-conditions) on Wiley Online Library for rules of use; OA articles are governed by the applicable Creative Commons License

Yuwei Zhang received his Ph.D. degree in Mechanical Engineering at Texas A&M University in 2021. He is currently a postdoctoral associate in the Department of Material Science and Engineering at Texas A&M University. His research focuses on small-scale mechanical testing in the field of energy storage and conversion.

Timothy D. Brown received his Ph.D. in Materials Science & Engineering at Texas A&M University in 2019. Since then, he has worked with Prof. Stan Williams at Texas A&M and now with Suhas Kumar at Sandia National Labs on the development and exploitation of Local Activity theory in the design of neuromorphic and dynamical devices and systems. His research interests include further development of Local Activity theory into simple and useful device engineering principles, codesign of the entire compute stack to implement energy-efficient "software-in-hardware" paradigms, and investigation of new materials expressing nonlinear physics for neuromorphic applications.

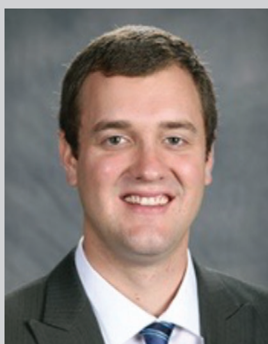

Matt Pharr is an associate professor and J. Mike Walker '66 Faculty Fellow in Mechanical Engineering at Texas A&M University with a courtesy appointment in Materials Science & Engineering. He serves as co-lead of Early-Stage Investigator Professional Development of REMIND, an Energy Frontier Research Center focused on advancing the fundamental science of neuromorphic computing funded by the United States Department of Energy. Recent distinctions include an NSF CAREER Award, a TEES Young Faculty Fellow Award, an Association of Former Students Distinguished Achievement in Teaching Award, and a TMS LMD Young Leaders Professional Development Award.

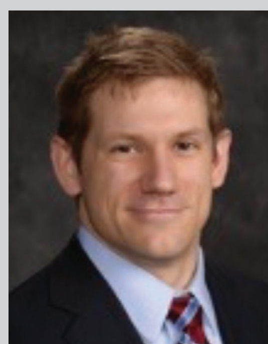

Patrick J. Shamberger earned his Ph.D. in Materials Science and Engineering from the University of Washington, Seattle, WA. Currently, he is an associate professor with the Department of Materials Science and Engineering at Texas A&M University. Prior to this, he served as a materials research engineer for the Air Force Research Lab in the Materials and Manufacturing directorate. His current research focuses on the development of reversible phase transformations for electronic and thermal applications. He is the recipient of several awards, including an NSF Career award from the Metals and Metallic Nanostructures program.

 © 2022 Wiley-VCH GmbH

Sarbajit Banerjee is the Davidson Chair Professor of Chemistry, Professor of Materials Science and Engineering, and Chancellor EDGES Fellow at Texas A&M University. He serves as the Executive Associate Director of REMIND, an Energy Frontier Research Center focused on advancing the fundamental science of neuromorphic computing funded by the United States Department of Energy. Recent distinctions include the TAMEST Edith and Peter O'Donnell Award in Science and the American Chemical Society Stanley C. Israel Regional Award for Advancing Diversity in the Chemical Sciences. He is a Fellow of the Royal Society of Chemistry and the Institute of Physics.

© 2022 Wiley-VCH GmbH

15214095, 2023, 37, Downloaded from https://onlinelibrary.wiley.com/doi/10.1002/adma.202205294 by Texas A&M University Library, Wiley Online Library on [06/12/2023]. See the Terms and Conditions (https://onlinelibrary.wiley.com/terms-and-conditions) on Wiley Online Library for rules of use; OA articles are governed by the applicable Creative Commons License